How do horizontal, frictional discontinuities affect reverse fault-propagation folding?

Emanuele Bonanno[1], Lorenzo Bonini[2,3], Roberto Basili[3], Giovanni Toscani[1], Silvio Seno[1]

1 Dipartimento di Scienze della Terra e dell'Ambiente, Università di Pavia, Pavia, ITALY

2 Dipartimento di Matematica e Geoscienze, Università di Trieste, Trieste, ITALY

3 Istituto Nazionale di Geofisica e Vulcanologia, Rome, ITALY

Corresponding author: *Lorenzo Bonini, e-mail address: lbonini@units.it*

Key words: reverse faults, fault-propagation fold, mechanical discontinuities, analog modeling

Highlights

- We focus on the role of thin frictional discontinuities in affecting the development of reverse faults
- Our method is based on wet clay analog models
- Our results show the impact of thin discontinuities on both propagation rate of new faults and on the development of the associated folds

Bonanno E., Bonini L., Basili R., Toscani G., Seno S. (2017). How do horizontal, frictional discontinuities affect reverse fault-propagation folding? *Journal of Structural Geology*, 102, 147-167, https://doi.org/10.1016/j.jsg.2017.08.001.

ABSTRACT

The development of new reverse faults and related folds is strongly controlled by the mechanical characteristics of the host rocks. In this study we analyze the impact of a specific kind of anisotropy, i.e. thin mechanical and frictional discontinuities, in affecting the development of reverse faults and of the associated folds using physical scaled models. We perform analogue modeling introducing one or two initially horizontal, thin discontinuities above an initially blind fault dipping at 30° in one case, and 45° in another, and then compare the results with those obtained from a fully isotropic model. The experimental results show that the occurrence of thin discontinuities affects both the development and the propagation of new faults and the shape of the associated folds. New faults 1) accelerate or decelerate their propagation depending on the location of the tips with respect to the discontinuities, 2) cross the discontinuities at a characteristic angle (~90°), and 3) produce folds with different shapes, resulting not only from the dip of the new faults but also from their non-linear propagation history. Our results may have direct impact on future kinematic models, especially those aimed to reconstruct the tectonic history of faults that developed in layered rocks or in regions affected by pre-existing faults.

1. INTRODUCTION

Shortening in the brittle crust is mostly accommodated by folding, fracturing, and faulting. These processes are intimately associated with one another and understanding their evolution through time is of paramount importance. Several kinematic models have been proposed to explain the relationships between faulting and folding (for a recent summary see McClay, 2011; and Brandes and Tanner, 2014). It is generally accepted that fault-related folding can be described by three end-member geometries: detachment folds, fault-bend folds, and fault-propagation folds (e.g. De Sitter, 1956; Dahlstrom, 1969; Suppe, 1983; Suppe and Medwedeff, 1984, 1990; Jamison, 1987; Chester and Chester, 1990; Mitra, 1990, 1992, 2003; Erslev, 1991; Fisher et al., 1992, Epard and Groshong, 1995; Poblet and McClay, 1996; Storti and Salvini, 1996; Hardy and Ford, 1997; Allmendinger, 1998; Suppe et al., 2004; Tavani et al., 2006; Hardy and Finch, 2007; Albertz and Lingrey, 2012;). Such three end-members, however, often represent different stages in the evolution of the same structure (e.g., Tavani and Storti, 2006; Storti et al., 1997). For instance, a contractional structure may form as a detachment fold, then propagate upward forming a ramp as a fault-propagation fold, and finally be deflected along a weak layer to operate as a fault-bend fold.

Although the evolution of detachment folds and fault-bend folds is mainly related to the friction of the surface where they propagate and to the intrinsic mechanical properties of the rocks involved, the propagation of a ramping fault is a more complex mechanism, mainly because a new slipping surface must be created. The development of new faults in an isotropic medium occurs through three successive phases (e.g., Anderson, 1942; Brace et al., 1966; Segall and Pollard, 1983; Cartwright et al., 1995; Mansfield and Cartwright, 2001; Scholz, 2002; Faulkner et al., 2006; Bonini et al., 2015): 1) a "nucleation" phase, during which small cracks form as a consequence of the applied stress, usually

with an *en echelon* arrangement; 2) a "creation" phase, when new fault planes form through the coalescence of previously formed cracks; and 3) a "propagation" phase, when a single fault grows through the connection of small cracks located at its outer tips. Note that during the propagation phase, both nucleation and creation phases continue to occur at fault tips, and that the general evolution of a fault is seldom a linear process. In an ideal isotropic case, however, the linear propagation of a new fault is often an accepted assumption. Different factors may affect this linearity in nature, including the different strength of the rocks involved in the faulting process, the non-uniformity of the stress field, the presence of fluids, the occurrence of background inherited fractures - which may not be homogeneously distributed in the faulted sequence - and pressure and/or heat flow variations. As a result, any deviation from the linearity of fault propagation impacts also on the associated folding.

Understanding the deviations from linearity in the propagation of a ramping fault is fundamental in many applications which use the activity (slip) of the fault as a basic parameter. In regions of active tectonics or in the external portion of orogenic belts, reverse faults or thrust-fault ramps are often blind or buried below piles of sediments, thus preventing any direct observation of the faults. Several kinematic models have been developed to relate the observations of deformation features (e.g. folded horizons, secondary brittle structures, uplifted and warped terraces, growth strata) to their causative fault and to investigate the evolution of the whole system through time (e.g., Suppe, 1983, Suppe and Medwedeff, 1990; Erslev, 1991; Epard and Groshong, 1995; Homza and Wallace, 1995; Hardy and Ford, 1997; Allmendinger, 1998; Mitra, 2002b, 2003; Allmendinger et al., 2004; Suppe et al., 2004; Vannoli et al., 2004; Jin and Groshong, 2006; Tavani et al., 2006; Storti and Salvini, 1996; Cardozo and Aanonsen, 2009; Cardozo et al., 2011; Maesano et al., 2013; Grothe et al., 2014; Maesano et al., 2015; Bergen et al., 2017). Other studies used different approaches based on mechanical modeling, such as boundary element methods (BEM; e.g. Roering et al., 1997), finite

element methods (FEM; e.g. Albertz and Lingrey, 2012), and discrete element methods (DEM; Hughes and Shaw, 2015).

Most studies agree that one of the main elements controlling the evolution of a ramping fault is the mechanical stratigraphy. Deviations from a linear evolution are commonly observed in layered rocks that are often characterized by alternating weak and strong layers. However, such behavior can be also associated with other mechanical heterogeneities. For example, interlayer surfaces or pre-existing fault planes located along the propagating fault trajectories represent mechanical discontinuities within the hosting rocks. How do these thin, frictional, mechanical discontinuities impact on the propagation of a ramping fault? To answer this question we analyze a set of analog models. Our goal is to highlight how initially horizontal thin, mechanical discontinuities deviate a propagating fault from its linear development. We study how such discontinuities affect the evolution of fault-propagation folds, first by reproducing the development of initially blind, reverse faults dipping at different angles. We then introduce one or two horizontal discontinuities above the fault initial tip to quantitatively analyze their role in affecting the development of the whole structure. Finally, we use our results to discuss the potential impact of our findings in the investigation of natural cases.

2. METHOD

Among the various fault dips that can be adopted for a preliminary experimental analysis we chose to reproduce the dips that are most commonly observed in areas of active reverse faulting. A global compilation of active reverse faults (Sibson and Xie, 1998) indicates two prominent peaks in the 25°-35° and 45°-55° intervals. Accordingly, we designed two experimental boxes with the master fault, i.e. the inclined surface along which the two rigid blocks slip with reverse kinematics, dipping at 30° and 45° (Fig. 1): the corresponding sets of experiments are named DIP30 and DIP45, respectively (Table 1). The two boxes are composed by two rigid blocks: one is fixed and represents the footwall, the other

is mobile and represents the hanging wall (Fig. 1). The analog material overlies these blocks and simulates the rock volume where the reverse fault is expected to propagate. In this setup the master fault is initially planar and blind.

As analogue material we used wet kaolin (#CC31 China Clay), which is widely used to analyze faulting and folding processes in scaled experiments (e.g. Withjack et al., 1990; Miller and Mitra, 2011; Mitra and Miller, 2013; Cooke et al., 2013; Bonini et al., 2014a; Bonini et al., 2016a). Several peculiarities make the kaolin especially suitable for our purpose: 1) its mechanical properties can be easily assessed by measuring the water content of the mixture and by imposing a specific strain rate; 2) thin mechanical discontinuities can be easily introduced by cutting the clay pack; 3) the small size of clay particles allows for a very high resolution of strain observations, especially those related with faulting and fracturing.

2.1. Scaling

A proper analog experiment is subject to specific scaling rules that must be representative of a natural setting (Hubbert, 1937; Hubbert, 1951; Ramberg, 1981). As recalled earlier, the mechanical behavior of wet kaolin depends mainly on its water content and strain rate (e.g., Eisenstadt and Sims, 2005; Cooke and van der Elst, 2012). In this study we used a mixture of clay with a 60% water content by mass, resulting in a density of 1.65 g/cm^3. It follows that we may assume a cohesion in the range 50 to 120 Pa (Eisenstadt and Sims, 2005) and a friction coefficient of 0.6 (Henza et al., 2010). To ensure a proper rheological behavior during the experiments we adopted a 0.02 mm/s hanging wall speed (Cooke and van der Elst, 2012). As a natural target we assumed a rock with a density of 2.5 g/cm^3 and a cohesion in the range 10-20 MPa. Hence, the scaling relationship can be calculated as:

$$\frac{c_m}{c_n} = \frac{\rho_m}{\rho_n}\frac{l_m}{l_n} \quad (1)$$

where c is the cohesion, ρ is the density and l is the length. The subscripts m and n denote the analogue model and the natural target, respectively. Solving Eq. 1 for the length of the models gives

$$l_m = l_n \frac{\rho_n}{\rho_m} \frac{c_m}{c_n} \quad (2)$$

and using the maximum and minimum values of the kaolin cohesion we obtain that 10 mm in our model correspond to about 0.1-1.0 km in nature. Hence, the clay cake placed above the two rigid blocks was made 50 mm-thick, representing 0.5-5.0 km in nature.

2.2. Modeling strategy

To analyze the impact of the presence of thin, horizontal, mechanical discontinuities onto the development of reverse faults and related folds we introduced such discontinuities in our models by cutting the clay cake with an electrified probe before moving the hanging wall block. This technique allows us to precut the wet clay pack without modifying its mechanical properties (Cooke et al., 2013; Bonini et al., 2014a; Bonini et al., 2015; Bonini et al., 2016a). We thus assume that friction along the precut is the same as that of natural faults forming in the wet kaolin.

For both experimental setups (DIP30 and DIP45) we tested three different configurations (Fig. 1; Table 1): 1) an isotropic case (_ISO), i.e. a single clay layer without any precut; 2) a case where there is only one precut in the middle of the clay pack (_1PC), thereby forming two clay layers; 3) a case where two evenly spaced precuts have been introduced (_2PC), thereby forming a three-layer clay pack. To test the repeatability of the processes and to handle the data statistically we replicated each configuration three times. The isotropic experiments serve as reference for all the others. Models with one precut provide information on how new faults interact with a horizontal discontinuity and how this interaction impacts on the folding process. Models with two precuts allow us to observe what happens when the discontinuity is closer to the initial tip of the master fault (the lower precut), and how the

increased number of discontinuities compares with the outcomes from the isotropic and single-precut models.

2.3. Data analysis

We collect data from our models by taking high-resolution photographs (at 18 megapixel resolution) of the lateral side of the experimental box at every 1 mm of displacement along the master fault plane. These images are analyzed every 5 mm in two main ways: 1) using the Move software (Midland Valley Exploration Ltd) to digitize faults, fractures, and folds; and 2) using the PIVlab software (Thielicke, 2014; Thielicke and Stamhuis, 2014), which adopts an optical technique in visible light (Digital Image Correlation method, D.I.C.) to aid the detection of particles movements and thus quantify the amount of deformation. All images are referenced to a fixed coordinate system so that structures from different models and at different shortening be compared objectively. Black quartz sand grains are placed on the side of the clay cake before starting the experiments to act as markers for the identification of displacement without modifying the mechanical properties of the clay mixture. The D.I.C in particular allows us to calculate the displacement field and the shear strain rate distribution.

One of the key elements to understand fault kinematics is the analysis of fault displacement, allowing a detailed reconstruction of fault evolution and the discrimination of the fault-related folding style (e.g., Williams and Chapman, 1983; Hedlund, 1997; Tavani et al., 2006; Hughes and Shaw, 2014). The ratio between propagation and slip (P/S) of a fault is another widely used parameter that allows the fault-related folding evolution to be analyzed in detail, in particular using methods based on the trishear theory (e.g., Erslev, 1991; Hardy and Ford, 1997; Allmendinger, 1998). By varying the P/S ratio we can restore different fold shapes associated with propagating faults, leaving all other parameters such as the fault dip or the fault tip position unchanged, (e.g., Allmendinger and Shaw, 2000). Our experimental approach provides data about the displacement distribution along the fault and

about the propagation of the fault through time. The latter is particularly important because the propagation rate of a fault can hardly be observed in nature, and also because fault propagation models are mainly based on the analysis of the displacement distribution along the fault from markers in the hanging wall and footwall. To extract data such as fault length and P/S ratio while the fault grows during the experiments we measure the coordinates of the upper tip point of the main new faults every 5 mm of total displacement imposed on the master fault. The retained fault upper tip position is the average of the three realizations of each experimental configuration. Many new faults form during the experiments, but we collect these data only about the main faults, i.e. those showing a significant change of the velocity field and along which the shear strain rate is larger (Fig. 2a), excluding secondary faults and fractures. When multiple faults show significant activity we assume the most developed one, i.e. the longest one, as the main fault.

Another interesting piece of information is the angle formed between the direction of the propagating faults and the slope of the discontinuity at its inflection point (Fig. 2b), which we refer to as Angle Of Incidence (AOI). The direction of new faults is measured as the up-dip projection of the line connecting the tip of the master fault and the tip of the main new propagating faults. The slope of the inflection point is obtained first by fitting the line drawing of precuts (sampled at regular intervals of 10 mm) with a spline function, then by calculating the first derivative of these curves. The average of the angle of incidence measured from the three experiments for each configuration is retained for further analyses.

Finally, to investigate the evolution of folds associated with fault propagation we inspect the topographic surface of the experiments during deformation every 5 mm of displacement on the master fault. Similarly to the other observations described above, we use data from three experiments for each configuration and retain the average. To this end we sample the height of each model surface at a

regular spacing of 10 mm, then fit these data with a spline function to obtain a synthetic curve representing the fold shape at each deformation step (Fig. 2c).

3. EXPERIMENTAL RESULTS

We present here the main features observed in all the experiments. Specifically, we describe the geometry and development of faults and tensile fractures, the displacement field, and the shear strain rate distribution for all model configurations. For the sake of simplicity, in sections 3.1 and 3.2 we limit the description to one of the three series of experiments. The new faults formed in the isotropic experiments, in both the DIP30 and DIP45 configurations, reach the surface after about 40 mm of total displacement on the master fault. Considering that the specific goal here is to compare experiments with and without precuts, we describe the experiments with precuts only until we accumulate 40 mm of total slip even if no new faults have reached the surface at this displacement level. We subdivide the model evolution into two stages based on the amount of displacement imposed on the master fault: an Early Stage from 0 to 20 mm, and a Late Stage from 20 to 40 mm. The results in terms of fault propagation, angle of incidence (AOI) and fold evolution are obtained considering the three series of experiments for each configuration (see section 2.3 for explanations).

3.1. DIP30 EXPERIMENTS (ISO, 1PC, 2PC)

This section describes the results of experiments performed with a 30°-dipping master fault (DIP30_ISO, DIP30_1PC, and DIP30_2PC; Table 1), illustrating faults and fractures that are visually detected on the long side of the models (Fig. 3), the displacement field (Fig. 4), and the shear strain rate (Fig. 5) derived from D.I.C. analysis.

During the Early Stage, in DIP30_ISO the new faults nucleate at the tip of the master faults and develop with a shallow dip as they propagate forward until they become horizontal or even curve downward into the footwall (Fig. 3). At the end of the Early Stage, more new faults are formed in the hanging wall of the previous ones with progressively steeper dip (Fig. 3). In DIP30_1PC, during the Early Stage the new faults exhibit the same pattern as those seen in the isotropic case. In DIP30_2PC,

the new faults are fewer and reach the lower precut at the end of the Early Stage (Fig. 3). In DIP30_ISO the displacement field highlights a trishear zone, with the apex located at the upper tip of the steeper fault (Fig. 4). The low-angle faults and fractures located in the footwall border the lower edge of the trishear zone. This zone is preserved during the entire DIP30_ISO, whereas in DIP30_1PC and DIP30_2PC it appears segmented since the beginning of the Early Stage due to partial reactivation of the precuts, as pointed out by shear strain rate analysis (Fig. 5). In DIP30_2PC the new faults are deflected, and when they link with the lower precut the extent of slip along them increases (Fig. 4 and 5). Conversely, during the Early Stage of experiment DIP30_1PC the faults remain below the precut, so that the precut is not fully activated.

During the Late Stage, in DIP30_ISO the new faults continue to grow (Fig. 3). The activity of the faults having a dip similar to that of the master fault is prominent with respect to other faults, as testified by both the velocity field (Fig. 4) and the shear strain rate (Fig.5) analyses. In DIP30_1PC and DIP30_2PC the upward propagation of faults and fractures stops against precuts, though in DIP30_2PC some fractures cross the lower precut at the end of the stage. Also in DIP30_1PC and DIP30_2PC the activity of faults showing the same dip as that of the master fault is predominant, while the activity on the low-angle faults gradually decreases (Fig. 5). In DIP30_1PC and DIP30_2PC layer-parallel faults nucleate in front of the upward-propagating faults and within the layers, along the neutral surface of the blocks bordered by precuts and the free surface. In DIP30_1PC the layer-parallel faults form close to the neutral surface of the upper layer, i.e. the layer between the free surface and the precut. In DIP30_2PC, several layer-parallel faults form; first in the middle layer, i.e. the layer located between the two precuts, and then in the uppermost layer. Conversely, layer-parallel faults never appear in the isotropic experiment. The displacement field (Fig. 4) shows that the trishear zone progressively narrows as deformation increases in all three cases. Finally, the activity of precuts and layer-parallel faults produces a decoupling between the different layers. Notice that in DIP30_2PC an upward-

propagating fault overtakes the lower precut and promotes the transition of slip from the lower to the higher precut at the end of the Late Stage (Figs. 4 and 5). In DIP30_1PC, small, reverse faults propagate downward from the free surface just along the hinge of the footwall syncline (Fig. 3).

3.2. DIP45 EXPERIMENTS (ISO, 1PC, 2PC)

This section present the results of experiments performed with a 45°-dipping master fault (DIP45_ISO, DIP45_1PC, and DIP45_2PC; Table 1; Figs. 6, 7 and 8).

During the Early Stage of all DIP45 experiments new faults form at the tip of the master faults (Fig. 6) with shallower dip as they grow in a way similar to that observed in DIP30 experiments. In DIP45_ISO, a series of convex-up splays form with progressively steeper angle up to the dip of the master fault. Toward the end of the Early Stage a new fault having the same dip as that of the master fault nucleates at the neutral surface of the associated fold and propagates both downward and upward; small antithetic shear faults also form in its hanging wall. In DIP45_1PC and DIP45_2PC new faults reach roughly the same height within the clay body, though in DIP45_2PC when these new faults reach the lower precut some layer-parallel faults form in the middle layer (Fig. 6). The displacement field of all DIP45 experiments (Fig. 7) shows a trishear zone that is narrower than that seen in the corresponding DIP30 experiments. In DIP45_1PC and DIP45_2PC the trishear zone also appears to be segmented as a consequence of the partial reactivation of precuts (Fig. 8). Similarly to DIP30, the early low-angle faults border the lower edge of the trishear zone in all DIP45 experiments. In DIP45_2PC, layer-parallel faults nucleate in the hinge zone of the middle layer.

During the Late Stage, in DIP45_ISO the fault that formed in the middle of the clay cake connects with an upward-growing fault stemming from the tip of the master fault. Several new layer-parallel faults form in the hanging wall of the newly-formed main fault (Fig. 6). In DIP45_1PC and DIP45_2PC the new faults are deflected as they approach the precut (the lower precut in DIP45_2PC).

Layer-parallel faults form in the fold hinge zone within the middle/upper layer as they did in the DIP30 experiments, but they are more numerous. As suggested by the shear strain rate analyses, layer-parallel faults show the same shear strain rates as those of the segments reactivated along precuts (Fig. 8). Similarly to the DIP30 configurations, faults with the same dip as that of the master fault are prominent during this stage, while the activity of low-angle faults gradually decreases in all models (Fig. 8). In DIP45_1PC small fractures propagate downward from the free surface along the hinge of the footwall syncline. At the end of the Late Stage, in DIP45_1PC the new faults cross the precut, whereas in DIP45_2PC the new faults cross both precuts (Fig. 6).

3.3. FAULT PROPAGATION

This section presents data of the evolution of new faults described using their length and P/S from all the experiments (see Fig. 9). In DIP30_ISO, the propagation of the main new faults is rather linear with a total average P/S ratio equal to 2.3. The quite regular increase and decrease of the P/S ratio is indicative of the propagation and nucleation phase of the new faults (Figs. 9a, and 9c). In DIP30_1PC, the evolution of the length of the new faults is rather regular only up to 25 mm of total displacement (Fig. 9c), i.e. until the new faults reach the precut: hence, the propagation of new faults rapidly decreases because the new faults are deflected along the precut (Fig. 9c). The total average P/S ratio (1.6) is lower than that observed in the isotropic experiment. In DIP30_2PC, the P/S ratio increases rapidly to 4.7 up to 10 mm of total displacement, then decreases to 0.8 when reaching 15 mm of total displacement, then increases again up to 1.4 at the end of the experiments (Fig. 9a). In summary, when the new fault is below the precut, the propagation rate is faster than that observed in the isotropic case. When the new fault reaches the precut it is deflected along it and almost stops its propagation. Once the fault crosses the precut, it tends to the same P/S ratio of the isotropic case. Notice that the non-zero P/S ratio in the experiments with one or two precuts when the new fault

reaches them does not mean that the propagation of the fault has slowed down; rather it implies that the fault propagation has stopped against the precut while the system is still accumulating deformation due to increasing displacement on the master fault. In this case the change in P/S ratio means that the upper tip point of the new fault changes its position without increasing the length of the fault, and this point migration being located within the trishear zone.

The DIP45_ISO experiment shows a quite linear trend of the P/S ratio, its average being similar to that of DIP30_ISO (2.1 vs 2.3: Fig. 9e). Also in this case the increase and decrease of P/S ratio indicate the nucleation and propagation phases of new faults. In DIP45_1PC, the fault length is similar to that observed in the isotropic case (Figs. 9b and 9d). The _ISO and _1PC configurations evolve differently at 20 mm of displacement, when the new faults in DIP45_1PC approach the precut. At the end of DIP45_1PC, both the length of new faults and P/S ratio increase, approaching the values observed in DIP45_ISO. The difference in the average of P/S ratio in DIP45_ISO and DIP45_1PC is negligible (DIP45_ISO, P/S = 2.1; DIP45_1PC, P/S = 2.2; Fig. 9b). The general trend of the fault propagation is quite different if compared to the DIP30_1PC experiment (Fig. 9f), where the new faults remain below the precut until the end of the experiments with an almost regular trend. In the DIP45_2PC experiment, the extent of development of the new faults is smaller than that of the isotropic case except for their late activity (i.e. after 30 mm of total displacement). The length of new faults shows a trend similar to that of the experiments with one precut, i.e. they show a P/S ratio increase after they cross the precuts (Fig. 9b). This increase of the P/S ratio, however, occurs at different displacement values corresponding to the different times when the new faults cross the precuts. The DIP45_2PC are different from the DIP30_2PC at the final stage (Fig. 9g) because in the former new faults cross both precuts whereas in the latter they cross just the lower precut (Figs. 9g and 9j).

3.4. ANGLE OF INCIDENCE (AOI)

The previous section clearly illustrates that new faults in different experimental configurations cross the precuts at different values of total displacement. To understand the mechanisms leading to these different evolutionary trends we analyze the angle between the new faults and the precuts, i.e. the AOI (Figs. 2b and 10). To document the arrest of the new faults when their upper tip coincides with the precuts we measure the total length of the new faults starting from the hanging wall cutoff of the rigid block. By doing this we obtain the net length of the new faults.

In DIP30_1PC, the propagating faults are deflected along the discontinuity and new faults never cross it (Fig. 10a). The new faults reach the precut at 25 mm of total displacement and the AOI is 130°. At the end of the experiments the AOI drops to about 110° (Fig. 10a). In DIP30_2PC, the propagating faults reach the precut at 20 mm of total displacement and the AOI is 140°. Unlike the DIP30_1PC experiment, in DIP30_2PC the new faults cross the lower precut at the latest stages of deformation (after 35mm of total displacement) when the AOI is approaching 90° (Fig. 10b).

In DIP45_1PC the new faults reach the precut at 15 mm of total displacement and the AOI is about 120° (Fig. 10c). At 30 mm of total displacement and at an AOI of 90° the new faults cross the precut, implying that the stasis is very short relative to the 30° experiments. In DIP45_2PC the new faults reach the lower precut at 15 mm of total displacement and the AOI is about 115° (Fig. 10d). The stasis lasts until 20-25 mm of total displacement when the AOI is about 90°.

In summary the new faults are able to cross the precuts when the AOI is about 90°. This seems independent from the dip of the master fault or from the amount of total displacement.

3.5. FOLD EVOLUTION

This section presents data on the evolution of folds through a pairwise comparison of all the experiments (Fig. 11).In the experiments with the 30° dipping master fault the more open limbs are

those seen in the isotropic case. In DIP30_1PC and DIP30_2PC experiments, we generally observe that the presence of discontinuities decreases the interlimb angle, i.e. the forelimb is slightly steeper, except for the initial stages (Fig. 11a). This is more evident comparing the single models configurations (Figs. 11c, 11d, 11e). In the first stages of the experiments with one discontinuity, the forelimb is slightly gentler than in the isotropic case because during the early phase of these experiments the flexural reactivation of the precut tends to enlarge the fold shape. In the middle stages of this experiment, however, the shape changes from wider to tighter; this occurs when the propagating faults are deflected along the portion of the precut that is reactivated with a dextral sense of shear (Fig. 11a; see also Fig. 5). This mechanism also gives way to a horizontal translation of the fold hinge (Figs. 11a and 11c). The models with two precuts show a tendency similar to that of experiments with one precut (Figs. 11a and 11d). In detail, however, the horizontal translation of the fold hinge is less pronounced than in the experiments with one precut, and the forelimb is steeper (Fig. 11e). In general, neither in the experiments with one precut nor in those with two precuts the backlimb shows significant deviations with respect to the isotropic case (Figs. 11c and 11d).

In the DIP45 experiments the backlimb shows differences in the fold shapes between isotropic models and models with the precuts (Fig. 11b). In the latter, the backlimb difference with the isotropic case increases during deformation. (Figs. 11b, 11f, and 11g). As for the forelimb, it is steeper than in the isotropic cases, similarly to what is seen in the DIP30 experiments. Also in the DIP45 experiments the flexural reactivation of the discontinuities and the deflection of the propagating faults along them gives rise to a horizontal migration of the fold hinges (Figs. 11f, and 11g).

Comparing DIP_30 with DIP 45 models the isotropic experiments (Fig. 11i) differ significantly both in the backlimb (different vertical heights) and in the forelimb (different slope). In the experiments with one and two precuts (Fig. 11j, 11k), the differences in backlimb are substantially the same,

whereas in the forelimb they tend to decrease in models with one precut (Fig. 11j) and become negligible when two precuts are present (Fig. 11k).

4. DISCUSSION

The many differences between the isotropic models and the models with one or two precuts show how thin mechanical discontinuities - represented by precuts in our experiments - affect the evolution of fault-propagation folds as well as that of secondary brittle structures in a controlled environment. In particular, we observe that experiments with precuts differ from the reference isotropic experiment in terms of number, orientation, and propagation rate of new faults. Consequently, also the shape and evolution of the associated folds are different. To improve our understanding on how reverse faults evolve in the presence of such discontinuities in the real world, we compare the results from our experiments with common observations that are made in the investigation of natural cases. Then we analyze three different cases exploiting our findings.

4.1. Fault propagation

The experimental results on the development of new faults show how horizontal discontinuities (precuts) affect their evolution. In general, the propagation of new faults is faster when their upper tip is located below the precut, and accelerates as they approach the discontinuity (see section 3.3). When the new faults reach a discontinuity, they are deflected along it decreasing or even stopping their propagation. After crossing the discontinuity, the propagation rate tends to be more regular, i.e. similar to the propagation rate seen in an isotropic material. These observations are in agreement with those coming from analog models in extensional settings (Bonini et al., 2015) or inferred from mechanical models of reverse faults (e.g., Cooke and Pollard, 1997; Roering et al., 1997) and from field observation (Tavani et al., 2017). The acceleration of the propagation rate below a discontinuity is directly related both to the friction (e.g., Roering et al., 1997) and to the amount of slip along the fault (Bonini et al., 2015).

In all our experiments we observe that when new faults approach the discontinuities they are deflected along them. It is known that when a propagating fracture meets a thin, frictional discontinuity it may be stopped, it may be deflected, or it may be able to cross it. Such behavior depends on intrinsic properties of the discontinuity, i.e. its toughness and friction (Hutchinson, 1996; Roering et al., 1997; Xu et al. 2003; Wang and Xu, 2006). In our experiments only some portions of the discontinuities are reactivated, and these slipping portions change during the experiments. The shear strain rate analysis shows that new faults are deflected along the slipping portions of the discontinuities with the same sense of shear, whereas they are stopped where the slipping portion of the discontinuities has the opposite sense of shear (Figs. 5 and 8). Hence, the sense of shear along a discontinuity plays a key role on the development of approaching faults. The fault deflection process may also explain why many active reverse faults in nature remain blind (Moss and Ross, 2011). For example, we may speculate that the presence of horizontal discontinuities above the tip of a propagating fault decreases the likelihood for that fault to breach and hence to produce earthquake ruptures at the ground surface.

In some of our experiments we observe that new faults cross the discontinuities, but this seems to happen only when and where new faults are almost perpendicular to the discontinuity, i.e. when the angle of incidence is about 90°.

4.2. Angle of incidence (AOI), the critical angle, and the crossing point

From the shear strain rate analyses (Figs. 5 and 8) we note that the point where new faults cross the discontinuities corresponds not only to the inflection point of the deformed discontinuities but also to the point where the sense of shear changes from dextral (on the right-hand side of the model) to sinistral (on the left-hand side of the model). This is the point where the slip along discontinuities is null. In general, the models show that when the new faults cross the discontinuities the AOI is about 90°, which can be considered as the critical angle for all our configurations. These results can be used

when studying natural cases where fault location is controversial, debated, or unknown for lack of direct and unambiguous evidence of the fault geometry and extent. In seismic reflection data, for example, it is sometimes difficult to visualize or infer the fault traces and their tip points because seismic noise or disturbances (seismic disturbance zone) make any interpretation less objective in the vicinity of the faults (e.g. Kostenko et al., 2008; Hale, 2013; Iacopini et al., 2016). In these cases, along with the other factors controlling fault propagation (e.g. fault dip, slip rate, processes ahead of the fault tip), the critical angle may guide the interpretation, suggesting the point along a folded surface (discontinuity) where a propagating fault may be expected to cut through.

4.3. Folding evolution

The shape of the fault-related folds is one of the most widely used pieces of information to reconstruct the evolution of contractional structures, and their development is usually assumed as a linear process. Previous sections discussed the evolution of the new faults throughout the experiments with and without discontinuities (precuts) showing, among other observations, that the propagation rate of the new faults is variable depending on (i) their initial location, (ii) the number of discontinuities, and (iii) what portions of the precuts are reactivated during the experiments. Also, in the experiments with precuts we observe the formation of different kinds of secondary brittle structures (e.g., layer-parallel faults). The presence of discontinuities also affects the evolution of the folds associated with faulting.

Our results suggest that (i) backlimbs are rather insensitive to the activity of discontinuities, and that (ii) using the forelimb shape to derive fault parameters (dip, slip, etc.) can be misleading as mechanical discontinuities tend to conceal differences related to the dip of the ramping faults (Fig. 11). This occurrence has been observed also in studies based on mechanical models that have analyzed the role of weak layers or mechanically heterogeneous stratigraphy (e.g. Hardy and Finch, 2007; Albertz and Lingrey, 2012; Albertz and Sanz, 2012; Hughes and Shaw, 2015). This suggest that both thin

frictional discontinuities and thin weak layers impact on the relationships between faults and folds. These findings are of paramount importance for example in calculating the slip rates of natural faults or deriving fault geometries from the shape of folded horizons.

4.4. Natural systems

As an application of the experimental results, we consider three natural cases where thin discontinuities potentially played a role during the evolution of the ramping faults. The first case is located in Southern California, San Fernando Valley, where active reverse faults are propagating and, in some cases, interacting with each other. In particular, we focus on the causative thrust fault of the 1994, Northridge earthquake (Fig. 12a). This thrust is blind and SW-dipping and its upper termination in its eastern portion is located close to another thrust system, dipping in the opposite direction, comprising the source of the M_w 7.1, 1971, San Fernando Earthquake (e.g. Hauksson et al., 1995; Mori et al. 1995; Huftile and Yeats, 1996). In its western portion, the upper tip of the Northridge thrust is located close to an imbricate thrust system, the Santa Susana Fault (Fig. 12a). The steep attitude of the Santa Susana thrust ramps and the location of the upper tip of the Northridge thrust located in their synclinal area suggest that the Northridge thrust is a propagating fault (e.g. Davis and Namson, 1994). The upper part of San Fernando and Santa Susana thrust systems can be considered as thin mechanical discontinuities located above or near the upper termination of the Northridge thrust, as in our experimental setup. As shown by our experiments, the activity of the master fault (in this case the Northridge thrust) can be stopped by the discontinuities until it reaches the critical angle. According with our models, this critical angle should be 90°. The angle between the Northridge Thrust and the Santa Susana faults is higher than 90° and a stoppage of the Northridge upward propagation against these faults is feasible. We recall that our experiments show that flexural slip along the discontinuities occurs only when the propagating fault tip is below or coincident with the discontinuity (Figs. 5 and 8).

During the 1994 earthquake sequence some shallow aftershocks were located in the area of the Santa Susana thrust systems and a flexural reactivation of these structures has been suggested (e.g. Davis and Namson, 1994). Following our experimental observations, this is coherent with a propagating fault stopped or deflected along discontinuities. In the eastern area (CS#2 in Fig 12a), the angle between the Northridge and San Fernando thrusts is close to 90°, i.e. close to the critical angle, hence in this case we suggest that the San Fernando thrust does not currently represent an obstacle to the upward propagation of the Northridge thrust. The different interaction of the Northridge thrust with the structure dipping in the opposite direction can be confirmed also by looking at the different shape of the folds associated with the activity of the Northridge thrust and even by considering the distribution of coseismic slip observed during the 1994 earthquake sequence. The folds associated with the Northridge thrust exhibit a steeper forelimb in its western portion than in its eastern portion, similarly to the coseismic slip which was larger in the western area than in the eastern area (e.g. Carena and Suppe, 2002). In our experiments, when a propagating fault is below and close to a discontinuity it increases the propagation rate. In the Northridge case this implies that the fault could be more developed in the western area because of the presence and activity of pre-existing discontinuities (the Santa Susana fault system). In this view, these discontinuities favor the development of the propagating fault, that is not only larger but also more mature; in other words, the more slip accumulates on a fault, the more easily a coseismic rupture will propagate along that fault (e.g. Scholz, 2002).

The second case is located in the Po Plain, in Northern Italy (Fig. 12b). In this area some blind thrust faults are still active and generate significant earthquakes (e.g. Maesano et al., 2015), as testified by the 2012 Emilia earthquake sequence during which the activation of two thrust ramps produced two mainshocks of M_w 6.1 and M_w 6.0 (e.g. Burrato et al., 2012; Bonini et al., 2014b; Bonini et al., 2016b). The thrust systems in this region involve two decollement levels, depicting classical ramp-flat trajectories (Fantoni and Franciosi, 2010; Ahmad et al., 2014; Toscani et al, 2014; Turrini et al., 2014,

2016). At a basin scale, the stratigraphic setting is rather uniform but the evolution of the various thrust system is rather different (see geological cross-sections in Fig. 12b). In the western zone the deeper thrust ramps appear to be deflected along an upper weak layer (cross-section #3 in Fig. 12b), whereas in the eastern zone the deeper thrust ramps cross the upper weak layer or form a short flat portion (cross-section #4 in Fig. 12b). This different behavior does not appear to be related to the different dip of the thrust ramps because both 45° dipping and the 20-25° dipping ramps are deflected along the upper weak layer in the western area, whereas in the eastern area steeper and less steep ramps cross the upper weak layer. Also the total displacement along the deeper ramp is not much different. The main difference between the two areas is related to the presence or absence of a fault along the upper weak layer, i.e. a flat portion of a thrust system developing above the upper decollement. The lower thrust ramps are deflected in the areas where a fault is present in the upper weak layer (see cross-section #3 in Fig. 12). As shown by our experiments, the tendency of the new faults to be deflected along the discontinuity is related, among others, to slip along the structures; in other words, slip along the discontinuity promotes the deflection. This observation is confirmed in the buried thrust systems of the Po Plain, where the deeper, propagating faults appear to be deflected along the upper thrust system.

The last case is located in the Western Kunlun Mountains front/Tarim Basin, at the very western end of China (Fig. 12c). Multiple décollement levels are seen in this region (see D1 and D2 in Cross-section #5 in Fig. 12c) where a duplex system has developed (Wang et al., 2013). The outermost thrust ramp is the causative fault of the 2015, M_w 6.5, Pishan earthquake, testifying that these structures are active (Lu et al., 2016; Li et al., 2016). The thrust system developed along both décollements levels D1 and D2. The upper level (D2) is folded by the deeper one (D1) and a series of linking thrusts developed between them, thus depicting the duplex system (Lu et al., 2016). Also in this case the structures that developed below a fault plane appear to have been deflected along it, confirming the

observations made in the Po Plain in Italy and in our experiments, i.e. that propagating faults are easily deflected along fault-containing levels.

The buried duplex system of the Western Kunlun Mountains front and of the Tarim Basin illustrates how multiple reverse faults are sensitive to the presence of a mechanical discontinuity. In our experiments we find that new faults cross the discontinuities at a critical angle of about 90°. This occurred because we forced the master fault to be active throughout the experiment. In nature, especially in the most external sectors of contractional areas, a reverse or thrust fault is active until its activity maintains the critical shape of the entire system, for example if its activity is coherent with the Coulomb wedge dynamics (Chapple, 1978; Davis et al., 1983; Dahlen, 1984, 1990; Dahlen et al., 1984). The long-term activity of a thrust in a contractional wedge is mainly due to the friction along the basal detachment, the angle of internal friction of the material forming the wedge, the erosion, the syn-kinematic sedimentation, and the pore pressure. In a region with two decollements where a shallower and a deeper thrust system are acting, these factors may not allow a deeper thrust ramp to reach a critical angle with a shallower (roof) thrust because a younger thrust activates in the footwall of the older one before the critical angle is reached. As a consequence, a duplex system form. Our experimental results may suggest that a duplex system forms easily when the upper (roof) thrust develops before the deeper system (floor and link thrust) because the presence of a roof thrust facilitates the deflection of the link thrust.

In summary, comparing our experimental results with natural cases we notice that pre-existing fault planes act as thin, weak discontinuities, regardless of whether they are thrust ramps belonging to different thrust systems (e.g. San Fernando Valley in California) or shallower thrusts belonging to the same thrust system (e.g. Po Plain in Italy; Kunlun Mountains front and Tarim Basin in China). This is reasonable if we consider that a greater amount of stress is needed to induce slip along a weak layer rather than along a previously-formed fault which has already slipped. When we apply stress along a

weak layer where no slipping surface already exists, part of the energy must be used to produce small cracks (nucleation phase; see the introduction), then to connect them and finally to create a fault plane (creation phase) and propagate it (propagation phase) inducing slip. In a region where fault planes already exist the applied stress can "immediately" induce slip, almost skipping the first phases. This reasoning has a direct impact in a hypothetical evolutionary scheme, where new, ramping faults evolve in regions where previously formed faults exists or do not exists in their propagation zones (Fig. 13), giving rise to different propagation rates and folding shapes.

4.5. Implications for kinematic models

Two seminal papers of the early 1990s proposed different solutions to address the relationships between folds and faults when slip along the fault plane decreases to zero. The first paper was published by Suppe and Medwedeff (1990), who transferred the kink-fold model developed for studying fault-bend folding to the case of fault-propagation folding. Such an approach, however, could not account for curved fold surfaces and for systematic variations in the thickness and dip of syn-tectonic strata. The second paper was published by Erslev (1991), who proposed a different approach based on the observation that in some natural cases fold hinges tighten and converge downward to form a triangular zone. Erslev's study laid the basis for the trishear theory, that has since become extremely popular (e.g. Hardy and Ford, 1997; Allmendingeg, 1998; Zehnder and Allmendinger, 2000; Cardozo et al., 2003; Allmendinger et al., 2004, Cristallini et al, 2004; Jin and Groshong, 2006; Cardozo, 2008; Cardozo and Aanonsen, 2009; Welch et al., 2009; Cardozo et al., 2011; Liu et al., 2012; Pei et al., 2014; Zhao et al, 2017). The trishear theory predicts the presence of a triangular zone of distributed deformation whose apical angle is located on the tip of the propagating fault. In this triangular zone the displacement vectors vary linearly in magnitude and orientation - from a maximum in the hanging wall side, to zero in the footwall side (Allmendinger, 1998). The shape of the trishear zone is mainly

controlled by two parameters: the propagation-to-slip ratio (P/S) and the size of the apical angle (Hardy and Ford, 1997; Allmendinger, 1998).

In all our experiments we observe gradual variations of the displacement vectors, both in orientation and module, from the hanging wall to the footwall (Figs. 4 and 7), a thickening of the footwall zone near the fault (Figs. 3, 6, and 11), and a smooth profile of the folds (e.g. Fig. 11). Such observations are all reminiscent of the trishear theory. In the isotropic models a quite regular triangular zone at the tip of the propagating faults is visible throughout the experiments (Figs. 4 and 7). Hence, the trishear method can be successfully applied to cases displaying a limited variability of the mechanical properties of the rocks hosting the propagating faults, as already suggested by previous studies (Cardozo et al., 2003; Hardy and Finch, 2007; Albertz and Sanz, 2012; Hughes and Shaw, 2015). In the non-isotropic experiments the reactivation of precuts has a deep impact on the displacement pattern (Figs. 4 and 7), showing a gradual variation of the displacement vectors from the hanging wall to the footwall and the thickening of the footwall zone (Figs. 3, 6, and 11), but it is not easy to identify a regular triangular zone at the tip of the propagating fault. This is especially evident in the experiments with two precuts (Figs. 3 and 6). In sections 3.1 and 3.2 we named this zone as *segmented trishear zone*. Segmentation is more evident when the tip of the propagating fault is still below the precuts. When the propagating fault reaches the precut and is deflected along it, our models are reminiscent of a fault-bend folding style, where the reactivated precuts mimic the generation of flat portions in the fault system". Hence, in layered rocks the kinematic models based on kink-fold models could be successfully applied (e.g. Hughes and Shaw, 2015). Notice that a variation of the displacement vectors is still visible, which is a typical characteristic of the trishear theory. An alternative solution to the utilization of kinematic models based on the trishear theory also for layered rocks is to use the mechanical discontinuity as a lower boundary of the trishear zone, at least when the tip of the propagating fault coincides with the discontinuity. A similar solution has been recently

proposed by Zhao et al. (2017). A fundamental question concerning practical applications of the kinematic models remains unanswered, however: for how long does the tip of the propagating fault coincide with the encountered discontinuity? While searching for an answer we may recall that in the kinematic analyses based on the trishear theory it is possible to impose a P/S variation while the system evolves; our experiments suggest during which phases of fault evolution the P/S should decrease, when it can be assumed to be zero, and when it should increase.

5. Conclusions

Our experiments allowed us to shed light on the role of thin, initially horizontal, frictional discontinuities on the evolution of reverse faults and associated folds. Our results suggest that such role is related to the intrinsic properties of the discontinuities (e.g. friction, toughness), and to their tendency to be reactivated. In general, the reactivation of discontinuities occurs when the upper tip of a propagating fault lies below them, or coincides with them. This reactivation tends to decrease the apical angle of the folds with respect to an isotropic case (i.e. without discontinuities), generating steeper forelimbs. The reactivation of the discontinuities, their characteristic slip distribution and their sense of shear control the ability of a discontinuity to deflect or stop a propagating fault. We may conclude that a slipping discontinuity with the same sense of shear of an approaching fault tends to deflect it until a critical angle of incidence is reached. The angle between the plane of the propagating fault and the slope of the folded discontinuity at its inflection point (i.e. the inflection point between the hanging wall anticline and the footwall syncline) is the critical angle, which in our models always approaches 90°. The inflection point of the folded discontinuity is also the preferred point where the propagating fault crosses the discontinuities.

Although our results provide new clues for an improved understanding of the evolution of faults and fault-related folds, we recall that they are necessarily based on a limited number of cases with

intrinsic limitations (e.g. footwall and hanging wall simulated with two rigid blocks, number of the simulated discontinuities, and frictional properties of the discontinuity). To achieve a better understanding of the relationships between fault activity and pre-existing discontinuities, the approach and the analysis presented here must be applied to a larger number of models, encompassing a range of tectonic regimes and of natural cases.

ACKNOWLEDGMENTS

This work was supported by “Finanziamenti di Ateneo per Progetti Scientifici” - FRA 2015, P.I. L. Bonini. Midland Valley Ltd. is acknowledged for making available the Move software to the University of Pavia and to the University of Trieste (ASI — Academic Software Initiative). All data about the experiments will be provided upon request. Our thanks go to Gianluca Valensise for sharing his views on this work with us. The editor Toru Takeshita and the reviewers Nestor Cardozo and Stefano Tavani are gratefully acknowledged for their reviews and the constructive criticism that improved the quality of this paper.

TABLES

Table 1. Summary of the analog experiments presented in this study**.**

FAULT DIP	NUMBER OF PRECUTS	NUMBER OF MODELS	INITIALS	CLAY THICKNESS (mm)	PRECUT POSITION (distance from the base of the model; mm)
30°	0	3	DIP30_ISO	50	-
	1	3	DIP30_1PC	50	25
	2	3	DIP30_2PC	50	17 (lower) - 34 (upper)
45°	0	3	DIP45_ISO	50	-
	1	3	DIP45_1PC	50	25
	2	3	DIP45_2PC	50	17 (lower) - 34 (upper)

FIGURE CAPTIONS

Figure 1. Schematic representation of the experimental apparatus with two different setups: 30° clay box (left column), and 45°clay box (right column). a) and b) are the plan view of both boxes. c), d), e) f), g), h) show the side view for all the configurations, both isotropic and with precuts. Orange colour marks the mobile parts.

Figure 2. Data acquisition procedure: a) Fault propagation: combining velocity field, shear strain rate and faults and fractures analyses to obtain the tip coordinates of the most active main fault. We consider the total length of the new faults (denoted by solid lines) as the distance between the initial tip point of the master fault and the upper tip of the new faults. The net length of the new faults (denoted by dashed lines) is the distance between the hanging wall cut-off of the rigid block and the upper tip of the new faults. b) Procedure to establish the angle of incidence (see section 2.3 for explanation). c) Fold evolution: sampling of the free upper surface of the model at regular intervals (every 1 cm) for three experiments with the same configuration, and application of the smoothing spline function to the three curves to get the best fit (see section 2.3 for explanation).

Figure 3. Analysis of faults and fractures in experiments with master fault dipping 30° for three different configurations: isotropic (_ISO), one precut (_1PC), and two precuts (_2PC). Each row represents the development of faults and fractures at every increment of 5 mm displacement on the master fault. Red and black lines represent the newly- and previously-formed faults, respectively, at each successive increment of displacement (5 mm). Dotted lines indicate faults or fractures where the offset determination is uncertain. Black thin lines indicates the position of precuts.

Figure 4. Displacement field analysis in experiments with master fault dipping 30° for three different configurations: isotropic (_ISO), one precut (_1PC), and two precuts (_2PC). Each row shows the

displacement field after every 5 mm of displacement on the master fault. Black arrows represent the displacement vectors. The traces of faults, fractures, and precuts are also shown.

Figure 5. Shear strain rate analysis in experiments with master fault dipping 30° for three different configurations: isotropic (_ISO), one precut (_1PC), and two precuts (_2PC). Each row represents the shear strain rate calculated at each 5 mm of displacement on the master fault. Red and blue zones highlight dextral and sinistral sense of shear in the side view, respectively.

Figure 6. Analysis of faults and fractures in experiments with master fault dipping 45° for three different configurations: isotropic (_ISO), one precut (_1PC), and two precuts (_2PC). Each row represents an increment of 5 mm of displacement on the master fault. Red and black lines represent the newly- and previously-formed faults, respectively, at each successive increment of displacement (5 mm). Dotted lines indicate faults or fractures where the offset determination is uncertain. Black thin lines indicates the position of precuts.

Figure 7. Displacement field analysis in experiments with master fault dipping 45° for three different configurations: isotropic (_ISO), one precut (_1PC), and two precuts (_2PC). Each row shows the displacement field after every 5 mm of displacement on the master fault. Black arrows represent the displacement vectors. The traces of faults, fractures, and precuts are also shown.

Figure 8. Shear strain rate analysis in experiments with master fault dipping 45° for three different configurations: isotropic (_ISO), one precut (_1PC), and two precuts (_2PC). Each row reports the shear strain rate calculated each 5 mm of displacement on the master fault. Red and blue zones highlight dextral and sinistral sense of shear in the side view, respectively.

Figure 9. Propagation/slip ratio and fault length analysis: a) and b) P/S evolution for 30° and 45° dipping master fault, respectively; the average values of P/S of each configuration is also reported. c)

and d) fault length evolution for 30° and 45° dipping master fault, respectively. e), f), and g) P/S comparison 30° vs 45°. h), i), and j) Fault length comparison 30° vs 45°. Each line derives from the average of three experiments per type.

Figure 10. Evolution of the angle of incidence (AOI): a) and b) Experiments with master fault dipping 30°. c) and d) Experiments with master fault dipping 45°. The three red dots at every step of displacement indicate the length of new faults in the three experiments with the same setup. Red dashed lines represent the average at each step of the evolution of the length of new faults, and refer to the left vertical axis. Blue dashed lines indicate the evolution of the length of new faults of isotropic case (to be used as term of comparison). Grey lines indicate the variation of the AOI, and refers to the right vertical axis. Vertical, thick, grey bars mark the zone where the AOI is about 90°.

Figure 11. Fold evolution: Free surface evolution for a) DIP30 and b) DIP45 experiments, from zero to 40 mm of displacement. Each triplet of curves is relative to an interval of 5 mm of displacement. c), d) and e) Fold shape comparison of DIP30 experiments; f), g) and h) Fold shape comparison of DIP45 experiments. Each curve is the difference between the fold shapes of the two folds measured at that interval of displacement. i), j), and k) Comparison of experiments with the same configuration (isotropic, i; one precut, j; and two precuts, k) but with different master fault dip (30° vs 45°).

Figure 12. Naturel cases: a) Map view of the San Fernando Valley in southern California, and two cross section, located in the northern part, showing the structural setting of the Northridge thrust, the Santa Susana faults and the San Fernando thrust. Modified from Carena and Suppe (2002). b) Location map of the Po Plain in Italy; cross-section #3 and #4 shows the structural setting of the north-western and central areas respectively. Modified from Toscani et al. (2014) and Bonini et al. (2014b). c) Location map of the Western Kunlun Mountains front and Tarim Basin in China; cross-section #5

shows the deeper thrust system (to the left) and the shallower thrust system forming duplexes below the weak horizon D2 (modified from Li et al.;2016).

Figure 13. Hypothetical evolutionary scheme of two scenarios: a) the weak layer is not a pre-existing slipping surface. The propagation of a thrust creates distributed shear on it. The fault crosses the discontinuity at the stage 5. b) one of the two weak levels is a pre-existing slipping surface (shallow thrust system), the propagation of a new thrust causes the flexural slip reactivation and more slip is adsorbed by the discontinuity than in the previous case. The fault crosses the discontinuity at the stage 6.

REFERENCES

Ahmad, M.I., Dubey, A.K., Toscani, G., Bonini, L., Seno S., 2014. Kinematic evolution of thrust wedge and erratic line length balancing: insights from deformed sandbox models. International Journal of Earth Sciences, 103, 1, 329-347, doi:10.1007/s00531-013-0947-8.

Albertz, M., Lingrey, S., 2012. Critical state finite element models of contractional fault-related folding: part 1. Mechanical analysis. Tectonophysics 576–577, 133–149.

Albertz, M., Sanz, P.F., 2012. Critical state finite element models of contractional fault-related folding: part 2. Mechanical analysis. Tectonophysics 576–577, 150–170.

Allmendinger, R.W., 1998. Inverse and forward numerical modeling of trishear fault-propagation folds. Tectonics 17, 640–656.

Allmendinger, R.W., Shaw, J.H., 2000. Estimation of fault propagation distance from fold shape: implications for earthquake hazard assessment. Geology 28, 1099–1102.

Allmendinger, R.W., Zapata, T., Manceda, R., Dzelalija, F., 2004. Trishear kinematic modelling of structures, with examples from the Neuquén Basin, Argentina. In: McClay, K.R. (Ed.). Thrust Tectonics and Hydrocarbon Systems. AAPG Mem. 82, 356–371.

Anderson, E.M., 1942. The Dynamics of Faulting (lst edn). Oliver & Boyd, Edinburgh.

Bergen, K.J., Shaw, J.H., Leon, L.A., Dolan, J.F., Pratt, T.L., Ponti, D.J., Morrow, E., Barrera, W., Rhodes, E.J., Murari, M.K., Owen, L.A., 2017. Accelerating slip rates on the Puente Hills blind thrust fault system beneath metropolitan Los Angeles, California, USA. Geology, v. 45, p. 227–230, doi:10.1130/G38520.1.

Bonini, L., Di Bucci, D., Toscani, G., Seno, S., Valensise, G., 2014a. On the complexity of surface ruptures during normal faulting earthquakes: excerpts from the 6 April 2009 L'Aquila (central Italy) earthquake (Mw 6.3). Solid Earth 5, 389–408.

Bonini, L., Toscani, G., Seno, S., 2014b. Three-dimensional segmentation and different rupture behaviour during the 2012 Emilia seismic sequence (Northern Italy). Tectonophysics, doi: 10.1016/j.tecto.2014.05.006.

Bonini, L., Basili, R., Toscani, G., Burrato, P., Seno, S., Valensise, G., 2015. The role of pre-existing discontinuities in the development of extensional faults: An analog modeling perspective. Journal of Structural Geology 74. 145–158.

Bonini, L., Basili, R., Toscani, G., Burrato, P., Seno, S., Valensise, G., 2016a. The effects of pre-existing discontinuities on the surface expression of normal faults: Insights from wet clay analog modeling. Tectonophysics, doi:10.1016/j.tecto.2015.12.015.

Bonini, L., Toscani, G., Seno, S., 2016b. Comment on "The May 20 (MW 6.1) and 29 (MW 6.0), 2012, Emilia (Po Plain, Northern Italy) earthquakes: New seismotectonic implications from subsurface

geology and high-quality hypocenter location" by Carannante et al., 2015. Tectonophysics 688, 182-188.

Brace, W.F., Paulding, B.W., Scholz C., 1966. Dilatancy in fracture of crystalline rocks. Journal of Geophysical Research 71 (16), 3939–3953.

Brandes, C., Tanner, D.C., 2014. Fault-related folding: A review of kinematic models and their application. Earth-Science Reviews 138, pp. 352–370.

Burrato P., Vannoli P., Fracassi U., Basili R., Valensise G., 2012. Is blind faulting truly invisible? Tectonic-controlled drainage evolution in the epicentral area of the May 2012, Emilia-Romagna earthquake sequence (northern Italy). Annals of Geophysics, 55(4), 525-531, doi: 10.4401/ag-6182.

Cardozo, N., Bhalla, K., Zehnder, A.T., Allmendinger, R.W., 2003. Mechanical models of fault propagation folds and comparison to the trishear kinematic model. Journal of Structural Geology 25, 1–18.

Cardozo, N., 2008. Trishear in 3D. Algorithms, implementation, and limitations. Journal of Structural Geology 30, 327–340.

Cardozo, N., Aanonsen, S., 2009. Optimized trishear inverse modeling. Journal of Structural Geology 31, 546–560.

Cardozo, N., Jackson, C.A.L., Whipp, P.S., 2011. Determining the uniqueness of best-fit trishear models, Journal of Structural Geology 33, 1063–1078.

Carena, S., Suppe, J., 2002. Three-dimensional imaging of active structures using earthquake aftershocks: The Northridge thrust, California. Journal of Structural Geology 24, 887–904, doi:10.1016/S0191-8141(01)00110-9.

Cartwright, J.A., Trudgill, B.D., Mansfield, C.S., 1995. Fault growth by segment linkage - an explanation for scatter in maximum displacement and trace length data from the canyonlands grabens of SE Utah. Journal of Structural Geology 17 (9), 1319–1326.

Chapple, W.M., 1978. Mechanics of thin-skinned fold and thrust belts. Geological Society of America Bulletin, v. 89, no. 8, p. 1189–1198, doi:10.1130/0016-7606(1978)89<1189 :MOTFB>2.0.CO;2.

Chester, J.S., Chester, F.M., 1990. Fault-propagation folds above thrusts with constant dip. Journal of Structural Geology 12, 903–910.

Cooke, M.L., Pollard, D.D., 1997. Bedding-plane slip in initial stages of fault-related folding. Journal of Structural Geology 19 (3), 567–581.

Cooke, M.L., van der Elst, N.J., 2012. Rheologic testing of wet kaolin reveals frictional and bi-viscous behavior typical of crustal materials. Geophysical Research Letters 39, doi:10.1029/2011GL050186.

Cooke, M.L., Schottenfeld, M.T., Buchanan, S.W., 2013. Evolution of fault efficiency at restraining bends within wet kaolin analog experiments. Journal of Structural Geology 51, 180–192.

Cristallini, E.O., Giambiagi, L., Allmendinger, R.W., 2004. True three-dimensional trishear: a kinematic model for strike-slip and oblique-slip deformation. Geol. Soc. Am. Bull. 116, 938–952.

Dahlen, F.A., 1984. Non-cohesive critical Coulomb wedges: An exact solution. Journal of Geophysical Research, v. 89, no. B12, p. 10,125–10,133.

Dahlen, F.A., 1990. Critical taper model of fold-and-thrust belts and accretionary wedges. Annual Review of Earth and Planetary Sciences, v. 18, no. 1, p. 55–99.

Dahlen, F.A., Suppe, J., Davis, D., 1984. Mechanics of fold-and-thrust belts and accretionary wedges: Cohesive Coulomb theory. Journal of Geophysical Research, v. 89, no. B12, p. 10,087–10,101.

Dahlstrom, C.D.A., 1969. Balanced cross-section. Can. J. Sci. 6, 743–757.

Davis, D., Suppe, J., Dahlen, F.A., 1983. Mechanics of fold and thrust belts and accretionary wedges. Journal of Geophysical Research, v. 88, no. B2, p. 1153–1172, doi:10.1029/JB088iB02p01153.

Davis, T.L., Namson, J. S., 1994. A balanced cross-section of the 1994 Northridge earthquake, southern California. Nature 372, 167-169.

De Sitter, L.U., 1956. Structural Geology. McGraw-Hill, New York, 551 pp.

Eisenstadt, G., Sims, D., 2005. Evaluating sand and clay models; do rheological differences matter? Journal of Structural Geology 27, 1399–1412.

Epard, J.L., Groshong, R.H., 1995. Kinematic model of detachment folding including limb rotation, fixed hinges and layer-parallel strain. Tectonophysics 247, 85–103.

Erslev, E.A., 1991. Trishear fault-propagation folding. Geology 19, 617–620.

Fantoni, R., Franciosi, R., 2010. Tectono-sedimentary setting of the Po plain and Adriatic foreland. Rend. Lincei 21 (1), S197eS209. doi:10.1007/s12210-010-0102-4.

Faulkner, D.R., Mitchell, T.M., Healy, D., Heap, M.J., 2006. Slip on 'weak' faults by the rotation of regional stress in the fracture damage zone. Nature 444, 922–925.

Fisher, M.P., Woodward, N.B., Mitchell, M.M., 1992. The kinematics of break-thrust folds. Journal of Structural Geology 14, 451–460.

Grothe, P.R., Cardozo, N., Mueller, K., Ishiyama, T., 2014. Propagation history of the Osaka-wan blind thrust, Japan, from trishear modeling. Journal of Structural Geology 58, 79–94.

Hale, D., 2013. Methods to compute fault images, extract fault surfaces, and estimate fault throws from 3D seismic images. Geophisics 78, NO. 2, O33–O43.

Hardy, S., Finch, E., 2007. Mechanical stratigraphy and the transition from trishear to kink-band fault-propagation fold forms above blind basement thrust faults: a discrete-element study. Marine and Petroleum Geology 24, 75–90.

Hardy, S., Ford, M., 1997. Numerical modelling of trishear fault propagation folding. Tectonics 16, 841–854.

Hauksson, E., Jones, L.M., Hutton, K., 1995. The 1994 Northridge earthquake sequence in California: Seismological and tectonic aspects. Journal of Geophysical Research 100, 12335–12355.

Hedlund, C.A., 1997. Fault-propagation, ductile strain, and displacement-distance relationships. Journal of Structural Geology 19, 243–248.

Henza, A.A., Withjack, M.O., Schlische, R.W., 2010. Normal-fault development during two phases of non-coaxial extension: An experimental study. Journal of Structural Geology 32 (11), 1656–1667.

Hubbert, M.K., 1937. Theory of scale models as applied to the study of geologic structures. Geol. Soc. Am. Bull. 48, 1459–1520.

Hubbert, M.K., 1951. Mechanical basis for certain familiar geologic structures. Geol. Soc. Am. Bull. 62, 355–372.

Huftile, G.J., Yeats, R.S., 1996. Deformation rates across the Placerita (Northridge Mw = 6.7 aftershock zone) and Hopper Canyon segments of the western Transverse Ranges deformation belt. Bulletin of the Seismological Society of America, v. 86, no. 1, part B, p. 3–18.

Hughes, A.N., Shaw, J.H., 2014. Fault displacement distance relationships as indicators of contraction fault-related folding style. AAPG Bulletin 98, 227–251.

Hughes, A.N., Shaw, J.H., 2015. Insights into the mechanics of fault-propagation folding styles. Geol. Soc. Am. Bull. 127, 1752–1765.

Hutchinson, J.W., 1996. Stresses and Failure Modes in Thin Films and Multilayers, Notes for a DCAMM Course. Technical University of Denmark, Lyngby, 1–45.

Iacopini, D., Butler, R.W.H., Purves, S., McArdle, N., De Freslon, N., 2016. Exploring the seismic expression of fault zones in 3D seismic volumes. Journal of Structural Geology 89, 54–73. doi:10.1016/j.jsg.2016.05.005

Jamison, W., 1987. Geometric analysis of fold development in overthrust terranes. Journal of Structural Geology 9, 207–219.

Jin, G., Groshong, R.H., 2006. Trishear kinematic modeling of extensional fault-propagation folding. Journal of Structural Geology 28, 170–183.

Kostenko, O.V., Naruk, S.J., Hack, W., Poupon, M., Meyer, H.-J., Mora-Glukstad, M., Anowai, C., Mordi, M., 2008. Structural evaluation of column-height controls at a toe-thrust discovery, deep-water Niger Delta. AAPG Bull. 92, 1615–1638.

Li, T., Chen, J., Fang, L., Chen, Z., Thompson, J.A., Jia, C., 2016. The 2015 Mw 6.4 Pishan earthquake: seismic hazards of an active blind Wedge thrust system at the western Kunlun range front, northwest Tibetan Plateau. Seismol. Res. Lett. 87(3): 1-8.

Liu, C., Yin, H., Zhu, L., 2012. TrishearCreator: a tool for the kinematic simulation and strain analysis of trishear fault-propagation folding with growth strata. Comput. Geosci. 49, 200–206.

Lu, R., Xu, X., He, D., Liu, B., Tan, X., Wang, X., 2016. Coseismic and blind fault of the 2015 Pishan M_w 6.5 earthquake: Implications for the sedimentary-tectonic framework of the western Kunlun Mountains, northern Tibetan Plateau. Tectonics 35, 956–964, doi:10.1002/2015TC004053.

Maesano, F.E., Toscani, G., Burrato, P., Mirabella, F., D'Ambrogi, C., Basili, R., 2013. Deriving thrust fault slip rates from geological modeling: Examples from the Marche coastal and offshore contraction belt, Northern Apennines, Italy. Marine and Petroleum Geology 42, 122-134, doi:10.1016/j.marpetgeo.2012.10.008.

Maesano, F.E., D'Ambrogi, C., Burrato, P., Toscani, G., 2015. Slip-rates of blind thrusts in slow deforming areas: examples from the Po Plain (Italy). Tectonophysics 643, 8-25. doi:10.1016/j.tecto.2014.12.007.

Mansfield, C., Cartwright, J.A., 2001. Fault growth by linkage: observations and implications from analogue models. Journal of Structural Geology 23, 745–763.

McClay, K., 2011. Introduction to thrust fault-related folding, In: McClay, K., Shaw, J. H., Suppe, J. (Eds.), Thrust fault-related folding, AAPG Mem., 94, 1–19.

Miller, J.F., Mitra, S., 2011. Deformation and secondary faulting associated with basement-involved compressional and extensional structures. AAPG Bull 95 (4), 675–689.

Mitra, S., 1990. Fault-propagation folds: geometry, kinematic evolution, and hydrocarbon traps. AAPG Bull 74, 921–945.

Mitra, S., 1992. Balanced structural interpretations in fold and thrust belts, In: Structural Geology of Fold and Thrust Belts (S. Mitra and G. W. Fisher, eds), pp. 53–77. John Hopkins University Press, Baltimore.

Mitra, S., 2002b. Structural models of faulted detachment folds. AAPG Bull 86, 1673–1694.

Mitra, S., 2003. A unified kinematic model for the evolution of detachment folds. Journal of Structural Geology 25, 1659–1673.

Mitra, S., Miller, J.F., 2013. Strain variation with progressive deformation in basement-involved trishear structures. Journal of Structural Geology 53, 70–79.

Mori, J., Wald, D.J., Wesson, R.L., 1995. Overlapping fault planes of the 1971 San Fernando and 1994 Northridge, California earthquakes. Geophys. Res. Lett 22, 1033-1036.

Moss, R.E.S., Ross, Z., 2011. Probabilistic fault displacement hazard analysis for reverse faults. Bull. Seismol. Soc. Am. 101, no. 4, 1542–1553.

Pei, Y., Paton, D.A., Knipe, R.J., 2014. Defining a 3-dimensional trishear parameter space to understand the temporal evolution of fault propagation folds. J. Struct. Geol. 66, 284e297. http://dx.doi.org/10.1016/j.jsg.2014.05.018.

Poblet, J., McClay, K., 1996. Geometry and kinematics of single layer detachment folds. Am. Assoc. Petrol. Geol. Bull 80, 1085–1109.

Ramberg, H., 1981. Gravity, deformation and the Earth's crust. Academic Press, London.

Roering, J.J., Cooke, M.L., Pollard, D.D., 1997. Why blind thrust faults do not propagate to the earth's surface: Numerical modeling of coseismic deformation associated with thrust-related anticlines. J. Geophys. Res. 102, 11,901-11,912.

Scholz, C.H., 2002. The Mechanics of Earthquakes and Faulting, second ed. Cambridge University Press, New York, p. 471.

Segall, P., Pollard, D.D., 1983. Joint formation in granitic rock of the Sierra Nevada. Geol. Soc. Am. Bull. 94, pp. 563–571.

Sibson, R.H., Xie, G., 1998. Dip range for intracontinental reverse fault ruptures: truth not stranger than friction? Bulletin of the Seismological Society of America 88, 1014-1022.

Storti, F., Salvini, F., 1996. Progressive rollover fault-propagation folding: a possible kinematic mechanism to generate regional-scale recumbent folds in shallow foreland belts. Am. Assoc. Petrol. Geol. Bull 80, 174–193.

Storti, F., Salvini, F., McClay, K., 1997. Fault-related folding in sandbox analogue models of thrust wedges. Journal of Structural Geology 19, 583–602.

Suppe, J., 1983. Geometry and kinematics of fault-bend folding. Am. J. Sci. 283, 684–721.

Suppe, J., Medwedeff, D.A., 1984. Fault-propagation folding. Geol. Soc. Am. Bull. (Abstracts with Programs), 16, 670.

Suppe, J., Medwedeff, D.A., 1990. Geometry and kinematics of fault-propagation folding. Eclogae Geol. Helv. 83, 409–454.

Suppe, J., Connors, C.D., Zhang, Y., 2004. Shear fault-bend folding. In: Thrust Tectonics and Hydrocarbon Systems (K.R. McClay, ed.). Am. Assoc. Petrol. Geol. Mem. 82, 303–323.

Tavani, S., Storti, F., 2006. Fault-bend folding as an end-member solution of (double-edge) fault-propagation folding. Terra Nova 18, 270–275.

Tavani, S., Storti, F., Salvini, F., 2006. Double-edge fault-propagation folding: geometry and kinematics. Journal of Structural Geology 28, 19–35.

Tavani, S., Granado, P., Arbués, P., Corradetti, A., Muñoz, J.A., 2017. Syn-thrusting, near-surface flexural-slipping and stress deflection along folded sedimentary layers of the Sant Corneli-Bóixols anticline (Pyrenees, Spain). Solid Earth, 8, 405–419. doi:10.5194/se-8-405-2017.

Thielicke, W., 2014. The Flapping Flight of Birds – Analysis and Application, Phd thesis, Rijksuniversiteit, Groningen.

Thielicke, W., Stamhuis, E.J., 2014. PIVlab – Towards User-friendly, Affordable and Accurate Digital Particle Image Velocimetry in MATLAB. Journal of Open Research Software, 2(1):e30, doi: http://dx.doi.org/10.5334/jors.bl.

Toscani, G., Bonini, L., Ahmad, M. I., Di Bucci, D., Di Giulio, A., Seno, S., Galuppo, C., 2014. Opposite verging chains sharing the same foreland: kinematics and interaction through analogue models (Central Po Plain, Italy). Tectonophysics 633, 268-282. doi:10.1016/j.tecto.2014.07.019.

Turrini, C., Lacombe, O., Roure, F., 2014. Present-day 3D structural model of the Po Valley basin, Northern Italy. Mar. Pet. Geol. 56, 266–289. http://dx.doi.org/10.1016/j. marpetgeo.2014.02.006.

Turrini, C., Toscani, G., Lacombe, O., Roure, F., 2016. Influence of structural inheritance on foreland-foredeep system evolution: An example from the Po valley region (northern Italy). Mar. Pet. Geol. 77, 376–398. http://dx.doi.org/10.1016/j.marpetgeo.2016.06.022.

Vannoli, P., Basili, R., Valensise, G., 2004. New geomorphologic evidence for anticlinal growth driven by blind-thrust faulting along the northern Marche coastal belt (central Italy). Journal of Seismology 8, 297-312, doi:10.1023/B:JOSE.0000038456.00574.e3.

Wang, C.Y., Chen, H.L., Cheng, X.G., Li, K., 2013. Evaluating the role of syn-thrusting sedimentation and interaction with frictional detachment in the structural evolution of the SW Tarim basin, NW China: insights from analogue modeling. Tectonophysics 608, pp. 642–652.

Wang, P., Xu, L.R., 2006. Dynamic interfacial debonding initiation induced by incident crack. Int. J. Solids Struct. 43, 6535–6550.

Welch, M.J., Knipe, R.J., Souque, C., Davies, R.K., 2009b. A Quadshear kinematic model for folding and clay smear development in in fault zones. Tectonophysics 471, 186–202.

Williams, G., Chapman, T., 1983. Strains developed in the hanging walls of thrusts due to their slip/propagation rate: a dislocation model. Journal of Structural Geology 5, 563–571.

Withjack, M.O., Oloson, J., Peterson, E., 1990. Experimental models of extensional forced folds. AAPG Bull. 74, 1038e1054.

Xu, L.R., Huang, Y.Y., Rosakis, A.J., 2003. Dynamic crack detection and penetration at interfaces in homogeneous materials: experimental studies and model predictions. J. Mech. Phys. Solids 51, 461–486.Zehnder, A.T., Allmendinger, R.W., 2000. Velocity field for the trishear model. Journal of Structural Geology 22, 1009–1014.

Zhao, H., Guo, Z., Yu, X., 2017. Strain modelling of extensional fault-propagation folds based on an improved non-linear trishear model: A numerical simulation analysis. Journal of Structural Geology 95, 60–76.

Figure1

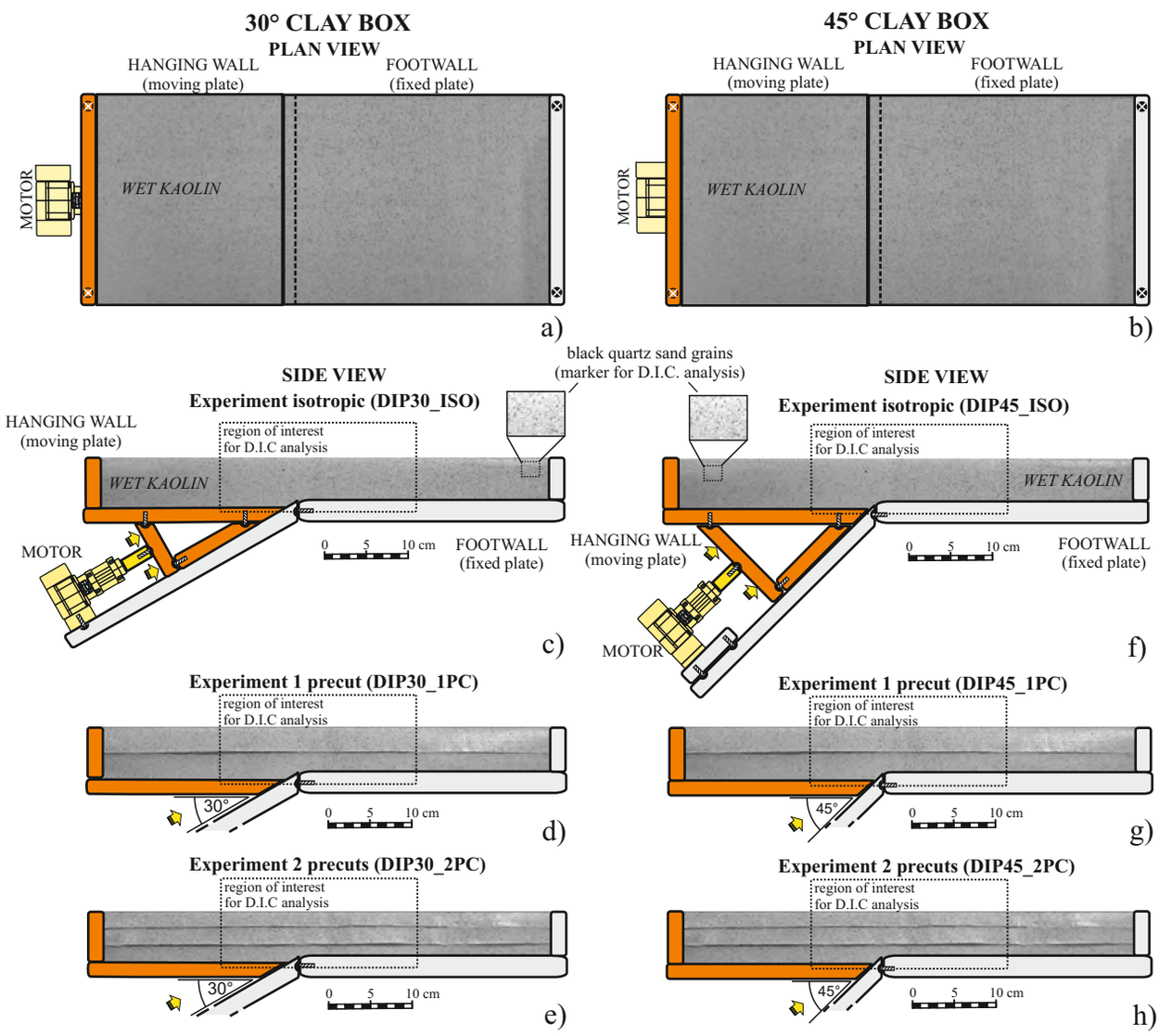

Figure 1. Schematic representation of the experimental apparatus with two different setups: 30° clay box (left column), and 45°clay box (right column). a) and b) are the plan view of both boxes. c), d), e) f), g), h) show the side view for all the configurations, both isotropic and with precuts. Orange colour marks the mobile parts.

Figure2

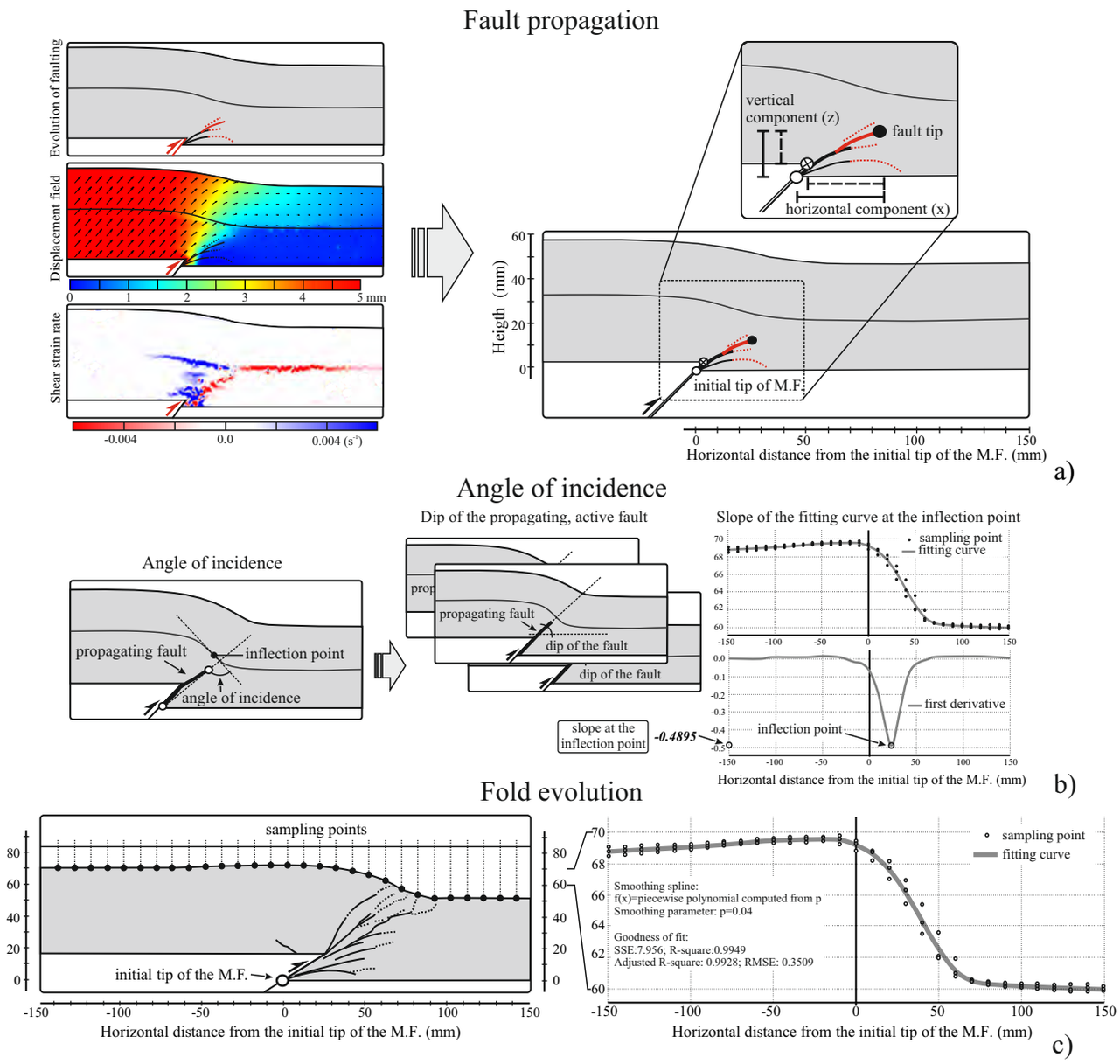

Figure 2. Data acquisition procedure: a) Fault propagation: combining velocity field, shear strain rate and faults and fractures analyses to obtain the tip coordinates of the most active main fault. We consider the total length of the new faults (denoted by solid lines) as the distance between the initial tip point of the master fault and the upper tip of the new faults. The net length of the new faults (denoted by dashed lines) is the distance between the hanging wall cut-off of the rigid block and the upper tip of the new faults. b) Procedure to establish the angle of incidence (see section 2.3 for explanation). c) Fold evolution: sampling of the free upper surface of the model at regular intervals (every 1 cm) for three experiments with the same configuration, and application of the smoothing spline function to the three curves to get the best fit (see section 2.3 for explanation).

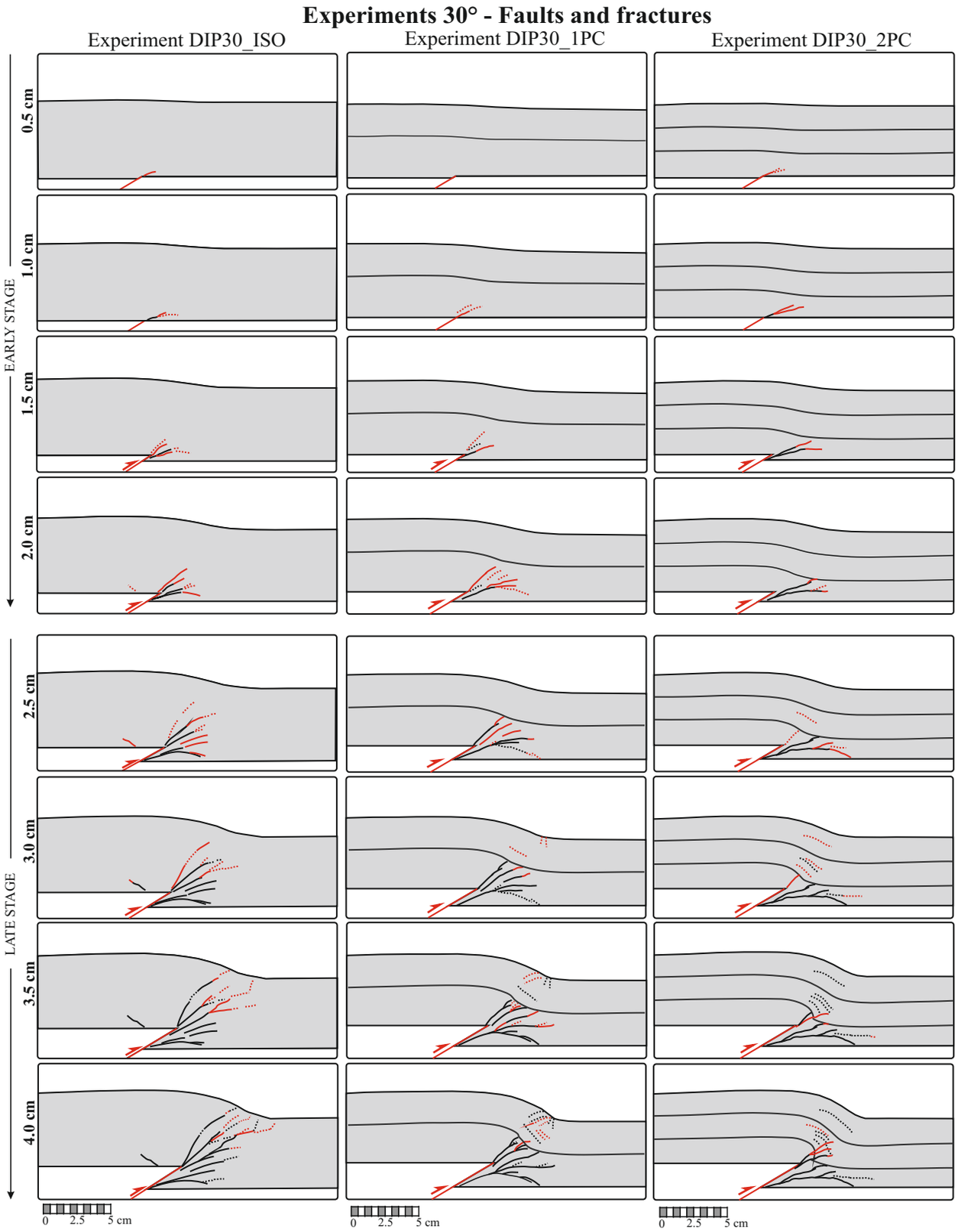

Figure 3. Analysis of faults and fractures in experiments with master fault dipping 30° for three different configurations: isotropic (_ISO), one precut (_1PC), and two precuts (_2PC). Each row represents the development of faults and fractures at every increment of 5 mm displacement on the master fault. Red and black lines represent the newly- and previously-formed faults, respectively, at each successive increment of displacement (5 mm). Dotted lines indicate faults or fractures where the offset determination is uncertain. Black thin lines indicates the position of precuts.

Figure4

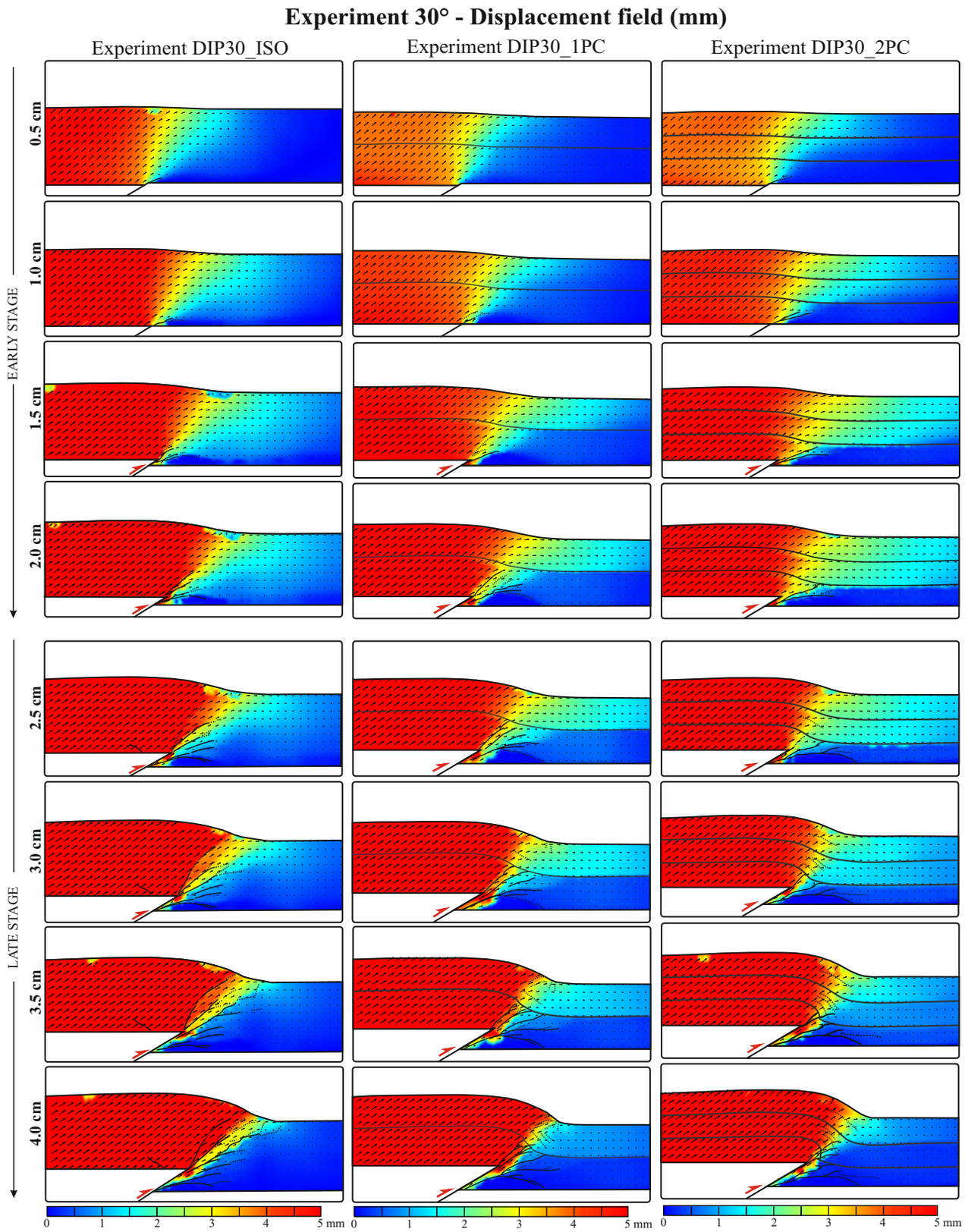

Figure 4. Displacement field analysis in experiments with master fault dipping 30° for three different configurations: isotropic (_ISO), one precut (_1PC), and two precuts (_2PC). Each row shows the displacement field after every 5 mm of displacement on the master fault. Black arrows represent the displacement vectors. The traces of faults, fractures, and precuts are also shown.

Figure5

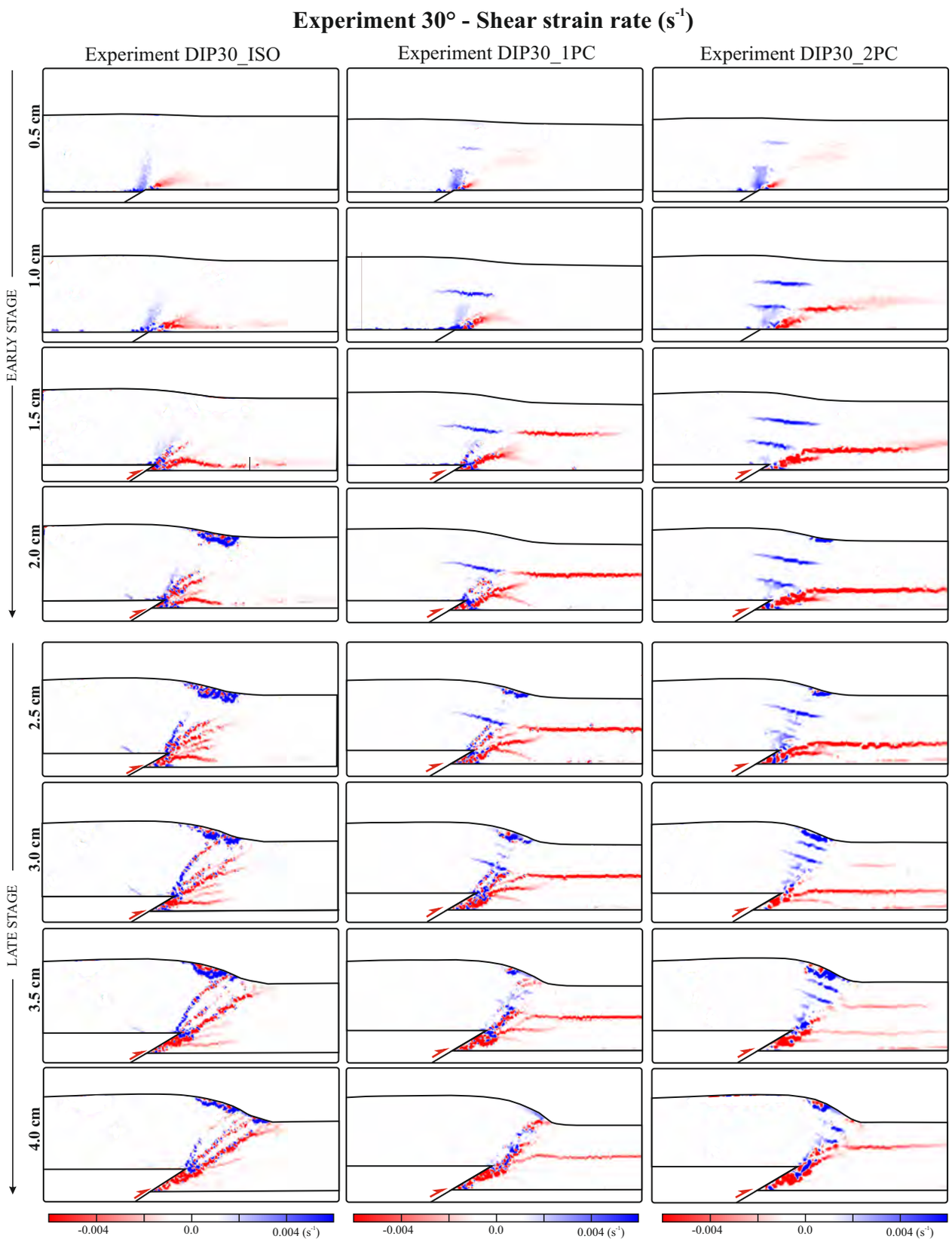

Figure 5. Shear strain rate analysis in experiments with master fault dipping 30° for three different configurations: isotropic (_ISO), one precut (_1PC), and two precuts (_2PC). Each row reports the shear strain rate calculated at each 5 mm of displacement on the master fault. Red and blue zones highlight dextral and sinistral sense of shear in the side view, respectively.

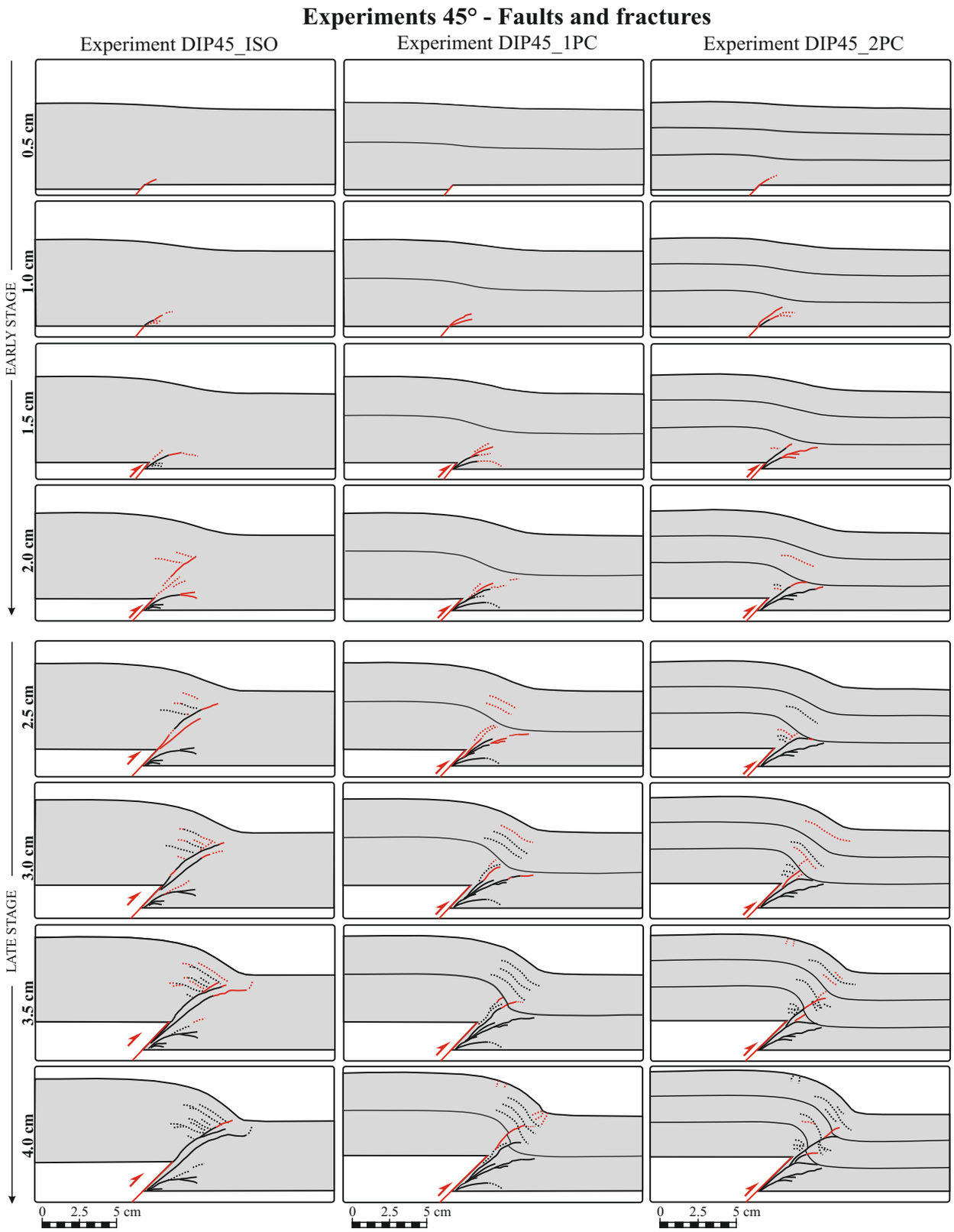

Figure 6. Analysis of faults and fractures in experiments with master fault dipping 45° for three different configurations: isotropic (_ISO), one precut (_1PC), and two precuts (_2PC). Each row represents an increment of 5 mm of displacement on the master fault. Red and black lines represent the newly- and previously-formed faults, respectively, at each successive increment of displacement (5 mm). Dotted lines indicate faults or fractures where the offset determination is uncertain. Black thin lines indicates the position of precuts.

Figure7

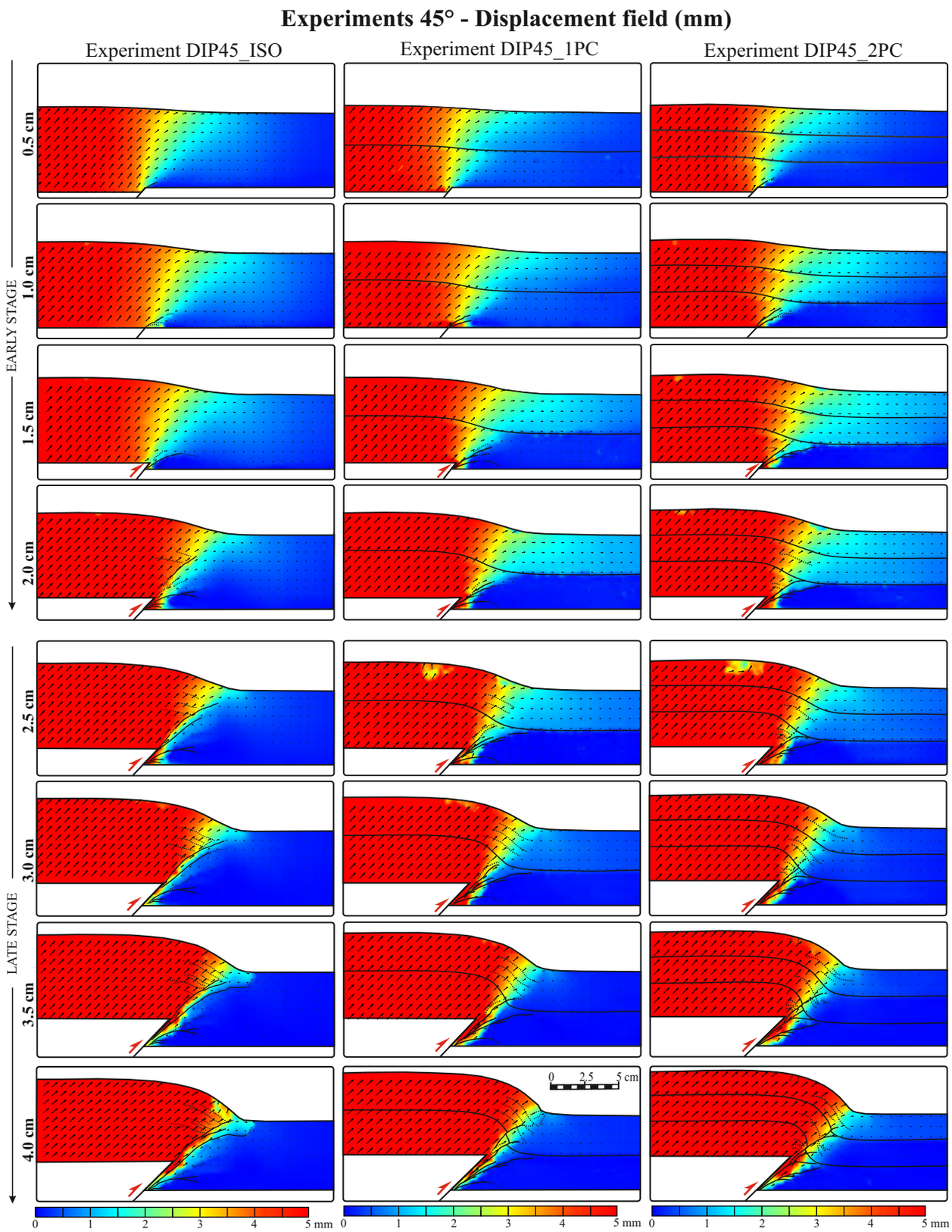

Figure 7. Displacement field analysis in experiments with master fault dipping 45° for three different configurations: isotropic (_ISO), one precut (_1PC), and two precuts (_2PC). Each row shows the displacement field after every 5 mm of displacement on the master fault. Black arrows represent the displacement vectors. The traces of faults, fractures, and precuts are also shown.

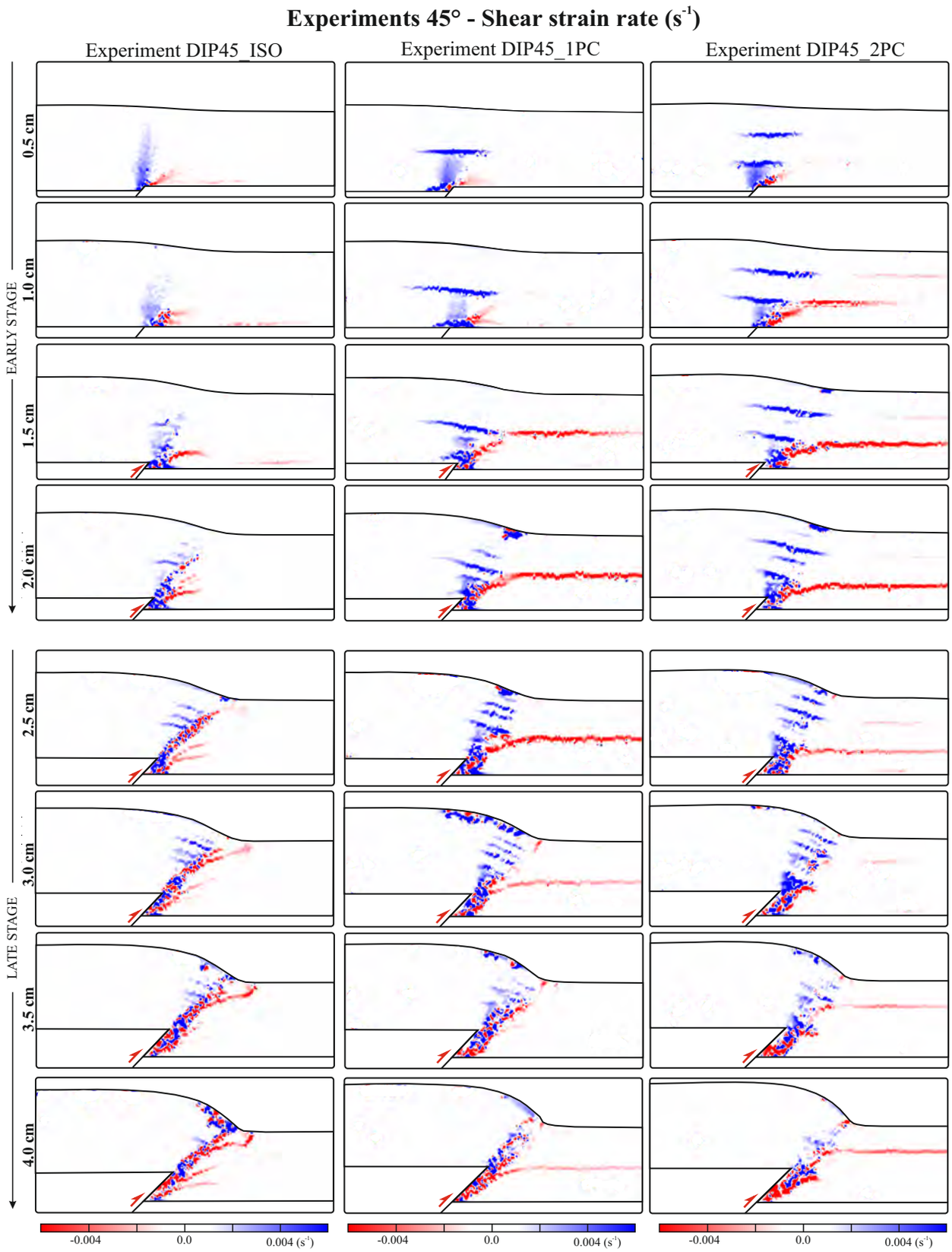

Figure 8. Shear strain rate analysis in experiments with master fault dipping 45° for three different configurations: isotropic (_ISO), one precut (_1PC), and two precuts (_2PC). Each row reports the shear strain rate calculated each 5 mm of displacement on the master fault. Red and blue zones highlight dextral and sinistral sense of shear in the side view, respectively.

Figure9

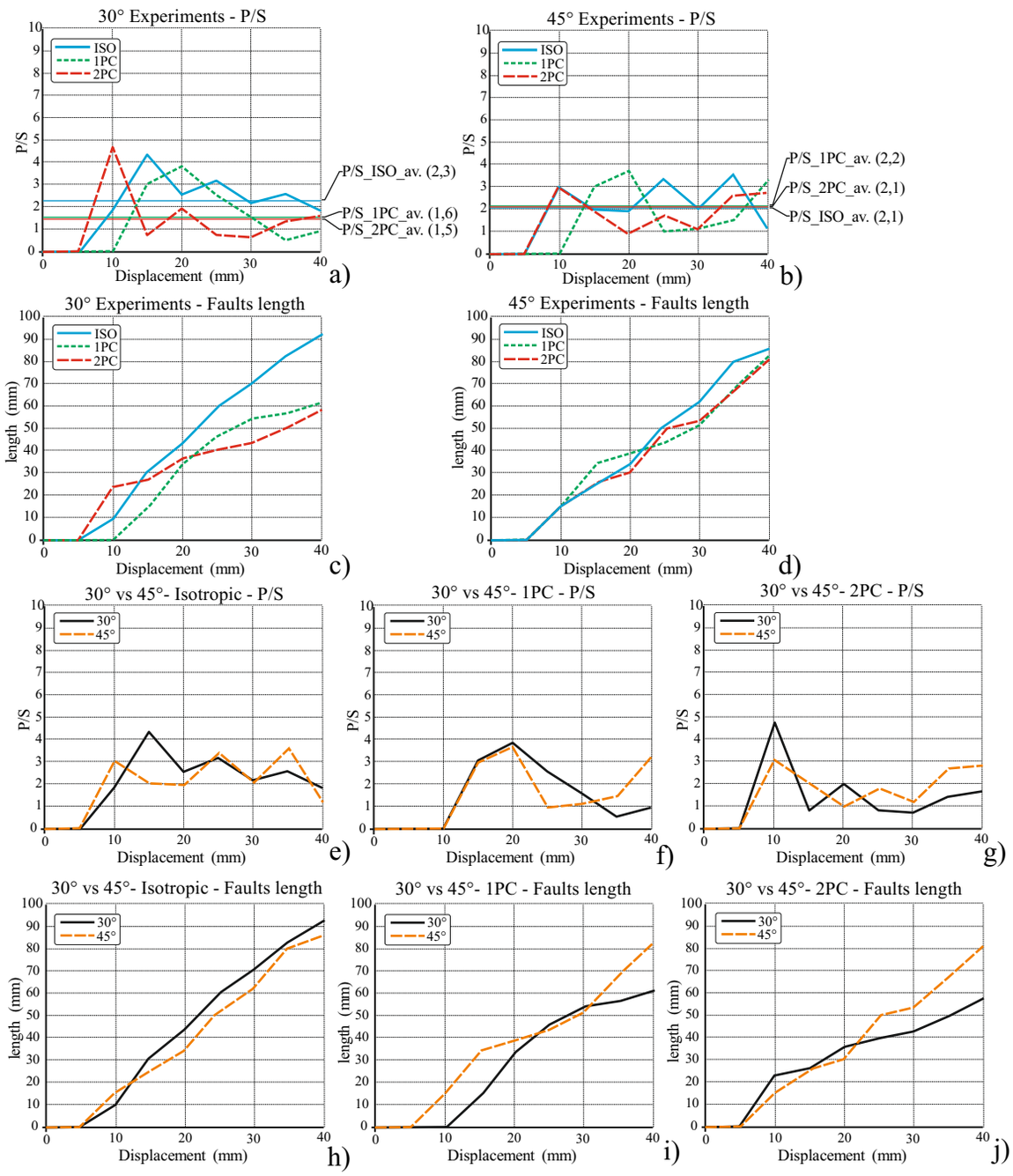

Figure 9. Propagation/slip ratio and fault length analysis: a) and b) P/S evolution for 30° and 45° dipping master fault, respectively; the average values of P/S of each configuration is also reported. c) and d) fault length evolution for 30° and 45° dipping master fault, respectively. e), f), and g) P/S comparison 30° vs 45°. h), i), and j) Fault length comparison 30° vs 45°. Each line derives from the average of three experiments per type.

Figure10

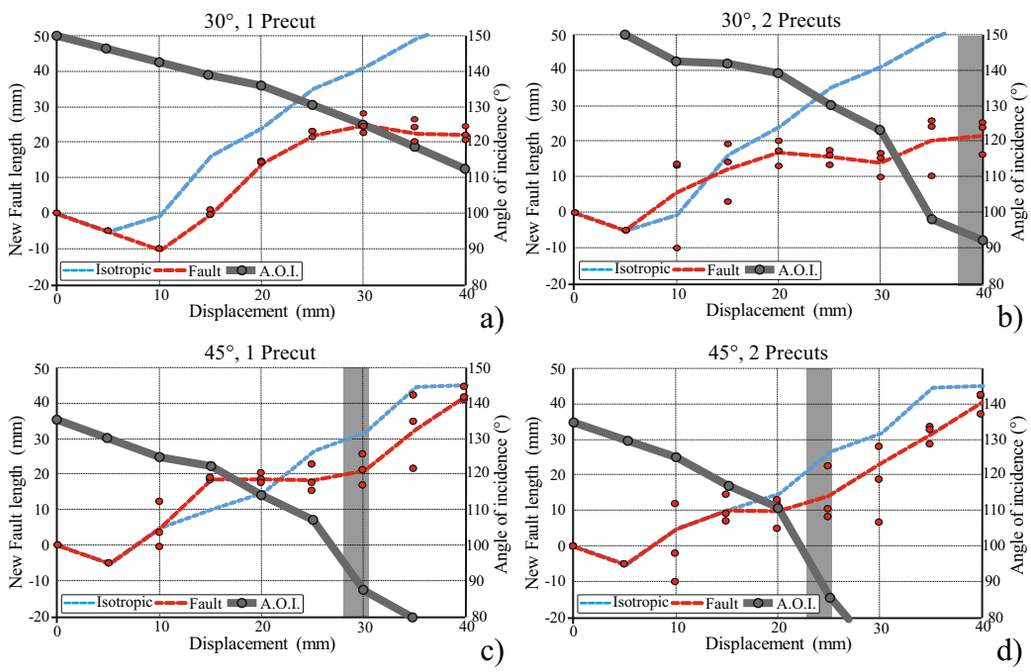

Figure 10. Evolution of the angle of incidence (AOI): a) and b) Experiments with master fault dipping 30°. c) and d) Experiments with master fault dipping 45°. The three red dots at every step of displacement indicate the length of new faults in the three experiments with the same setup. Red dashed lines represent the average at each step of the evolution of the length of new faults, and refer to the left vertical axis. Blue dashed lines indicate the evolution of the length of new faults of isotropic case (to be used as term of comparison). Grey lines indicate the variation of the AOI, and refers to the right vertical axis. Vertical, thick, grey bars mark the zone where the AOI is about 90°.

Figure11

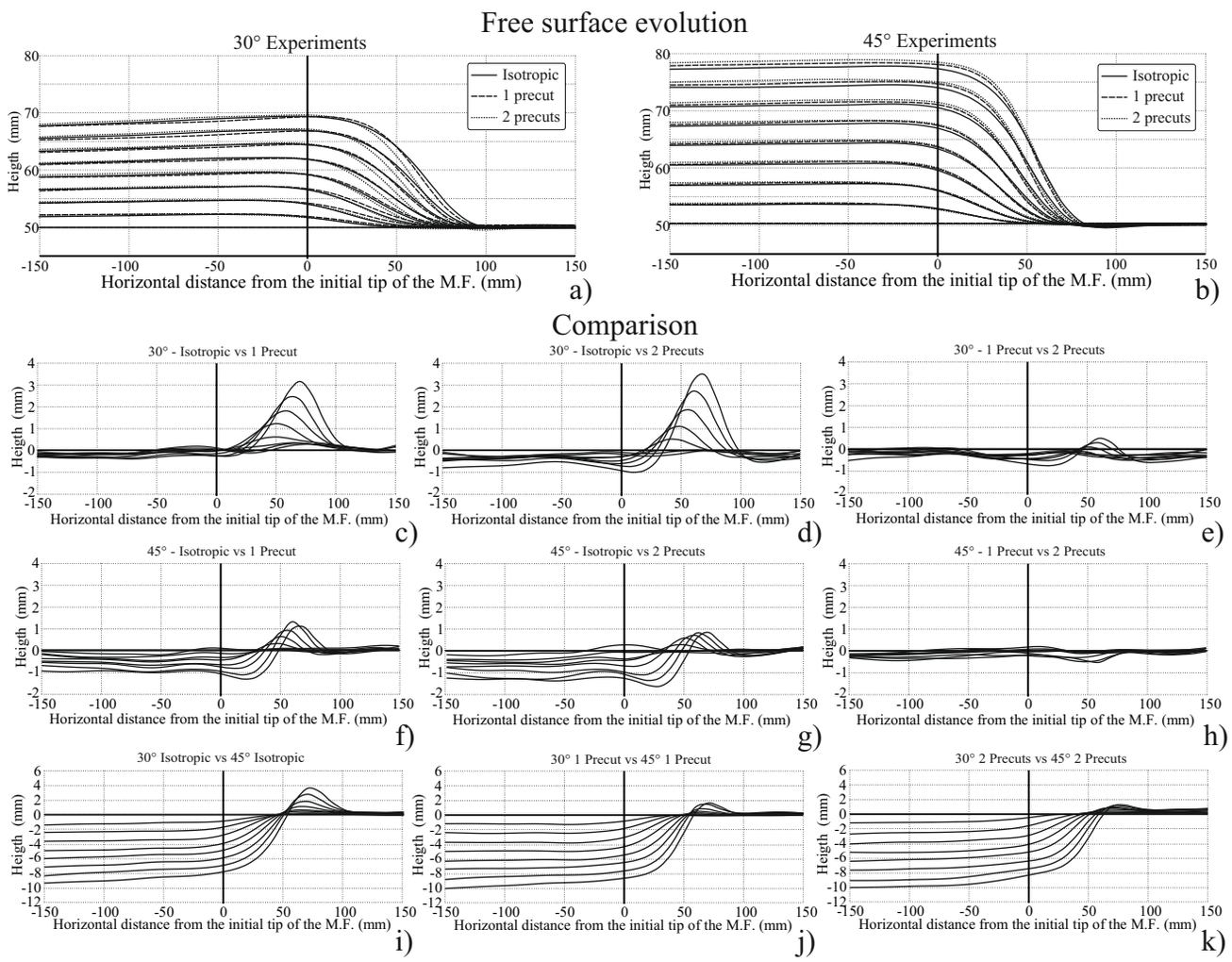

Figure 11. Fold evolution: Free surface evolution for a) DIP30 and b) DIP45 experiments, from zero to 40 mm of displacement. Each triplet of curves is relative to an interval of 5 mm of displacement. c), d) and e) Fold shape comparison of DIP30 experiments; f), g) and h) Fold shape comparison of DIP45 experiments. Each curve is the difference between the fold shapes of the two folds measured at that interval of displacement. i), j), and k) Comparison of experiments with the same configuration (isotropic, i; one precut, j; and two precuts, k) but with different master fault dip (30° vs 45°).

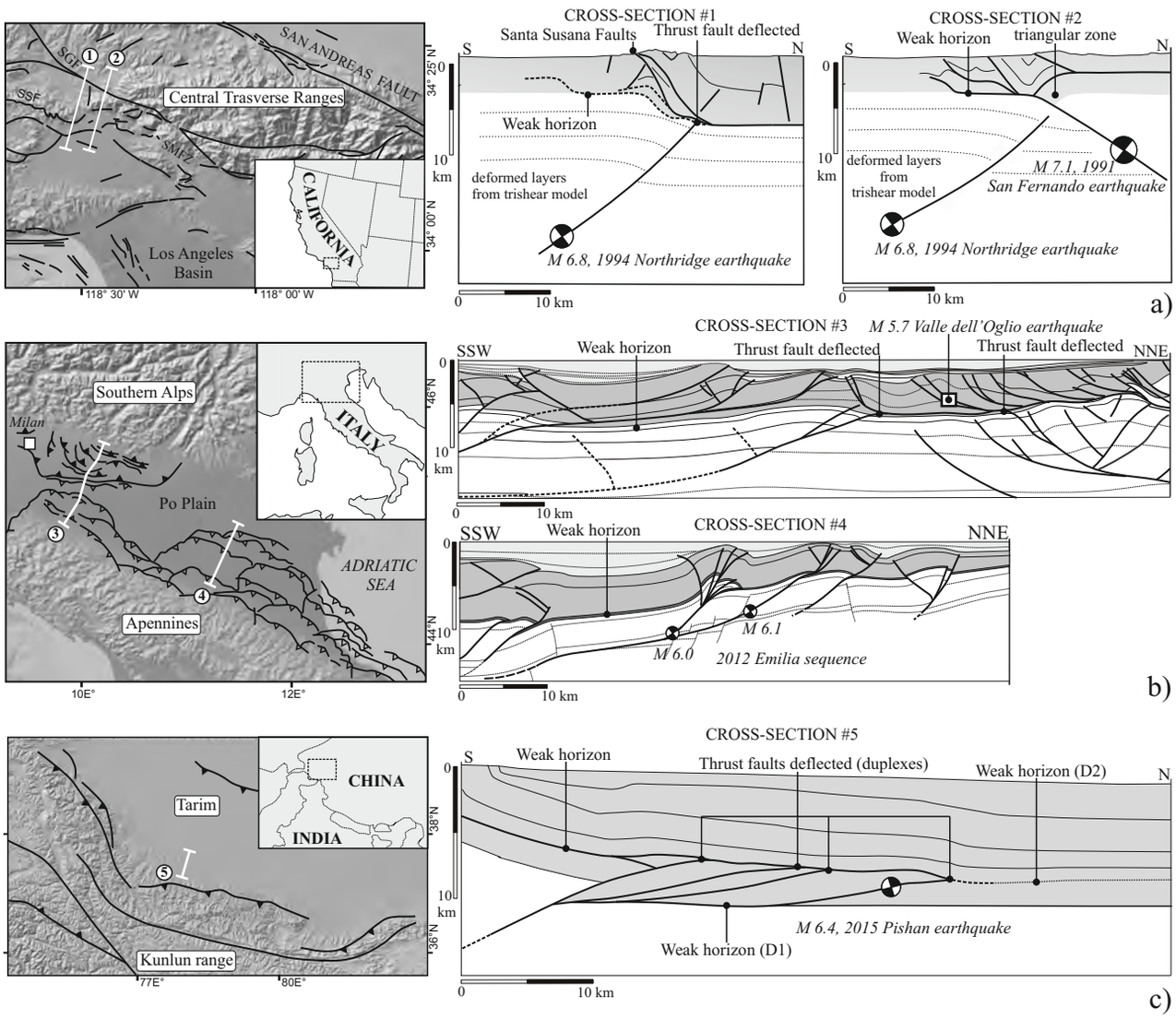

Figure 12. Naturel cases: a) Map view of the San Fernando Valley in southern California, and two cross section, located in the northern part, showing the structural setting of the Northridge thrust, the Santa Susana faults and the San Fernando thrust. Modified from Carena and Suppe (2002). b) Location map of the Po Plain in Italy; cross-section #3 and #4 shows the structural setting of the north-western and central areas respectively. Modified from Toscani et al. (2014) and Bonini et al. (2014b). c) Location map of the Western Kunlun Mountains front and Tarim Basin in China; cross-section #5 shows the deeper thrust system (to the left) and the shallower thrust system forming duplexes below the weak horizon D2 (modified from Li et al.;2016).

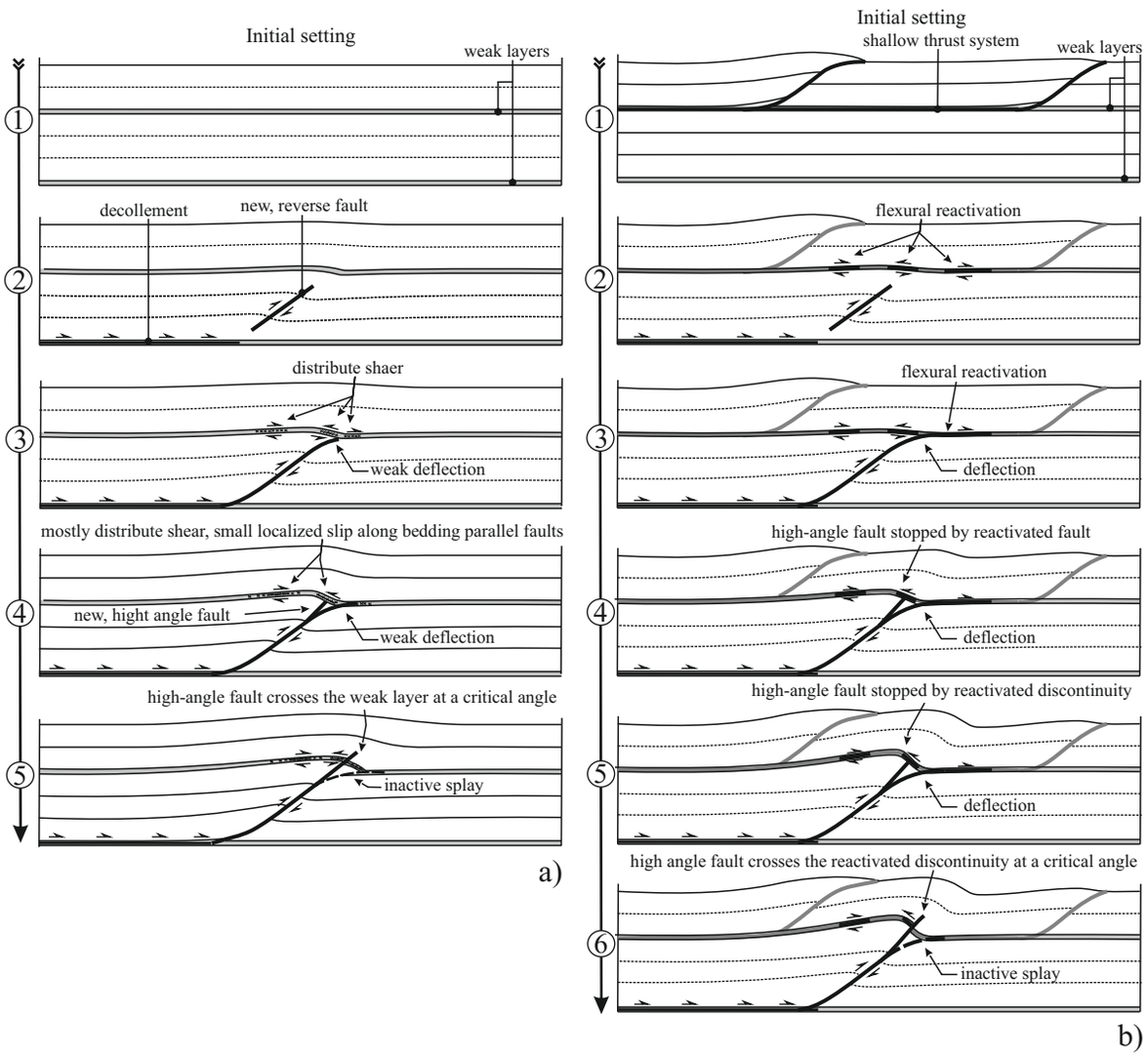

Figure 13. Hypothetical evolutionary scheme of two scenarios: a) the weak layer is not a pre-existing slipping surface. The propagation of a thrust creates distributed shear on it. The fault crosses the discontinuity at the stage 5. b) one of the two weak levels is a pre-existing slipping surface (shallow thrust system), the propagation of a new thrust causes the flexural slip reactivation and more slip is adsorbed by the discontinuity than in the previous case. The fault crosses the discontinuity at the stage 6.